Article

Experimental and Numerical Investigations of the Development of Residual Stresses in Thermo-Mechanically Processed Cr-Alloyed Steel 1.3505

Bernd-Arno Behrens [1], Jörg Schröder [2], Dominik Brands [2], Lisa Scheunemann [2], Rainer Niekamp [2], Alexander Chugreev [1], Mohammad Sarhil [2] and Sonja Uebing [2] and Christoph Kock [1,*]

[1] Institut für Umformtechnik und Umformmaschinen, Leibniz Universität Hannover (PZH), 30823 Garbsen, Germany; behrens@ifum.uni-hannover.de (B.-A.B.); chugreev@ifum.uni-hannover.de (A.C.)

[2] Institut für Mechanik, Abteilung Bauwissenschaften, Fakultät für Ingenieurwissenschaften, Universität Duisburg-Essen, 45141 Essen, Germany; j.schroeder@uni-due.de (J.S.); dominik.brands@uni-due.de (D.B.); lisa.scheunemann@uni-due.de (L.S.); rainer.niekamp@uni-due.de (R.N.); mohammad.sarhil@uni-due.de (M.S.); sonja.uebing@uni-due.de (S.U.)

* Correspondence: kock@ifum.uni-hannover.de

Abstract: Residual stresses in components are a central issue in almost every manufacturing process, as they influence the performance of the final part. Regarding hot forming processes, there is a great potential for defining a targeted residual stress state, as many adjustment parameters, such as deformation state or temperature profile, are available that influence residual stresses. To ensure appropriate numerical modeling of residual stresses in hot forming processes, comprehensive material characterization and suitable multiscale Finite Element (FE) simulations are required. In this paper, experimental and numerical investigations of thermo-mechanically processed steel alloy 1.3505 (DIN 100Cr6) are presented that serve as a basis for further optimization of numerically modeled residual stresses. For this purpose, cylindrical upsetting tests at high temperature with subsequently cooling of the parts in the media air or water are carried out. Additionally, the process is simulated on the macroscale and compared to the results based on the experimental investigations. Therefore, the experimentally processed specimens are examined regarding the resulting microstructure, distortions, and residual stresses. For the investigation on a smaller scale, a numerical model is set up based on the state-data of the macroscopic simulation and experiments, simulating the transformation of the microstructure using phase-field theory and FE analysis on micro- and meso-scopic level.

1. Introduction

During the manufacturing of components, various residual stress states may occur in the material because of the process. In the past, there have been several investigations of the relationship between forming parameters such as deformation state or temperature profile and resulting residual stresses by experiments and simulations; see for instance [1–3]. The work of [4] investigated process parameters, deformation state, and temperature time profile with special regard to the spring-back behavior after a

hot stamping process. It is noteworthy that the residual stresses resulting from metal-forming processes are generally known to have negative effects, regarding e.g., lifetime, so that avoidance or minimization during the manufacturing process is usually targeted instead of specifically influencing component properties. For example, positive effects on the fatigue life of components due to residual compressive stresses have already been achieved by the surface treatment process of shot peening applied as an additional process step [5]. The overall objective pursued in this paper is to analyze and adjust hot forming processes to achieve a favorable residual stress profile directly from the forming stage. To achieve defined material properties in the formed component, targeted cooling or heat treatment is necessary [6]. For example, quenching from the forging temperature is an energy-efficient way of tempering components [7]. Hot forming as a thermo-mechanically coupled process offers the potential for many adjustment parameters to influence residual stresses. As a consequence, complex material phenomena arising during the individual process steps interact and emphasize each other, decisively affecting the final component properties and making the virtual process design rather complicated, cf. Figure 1.
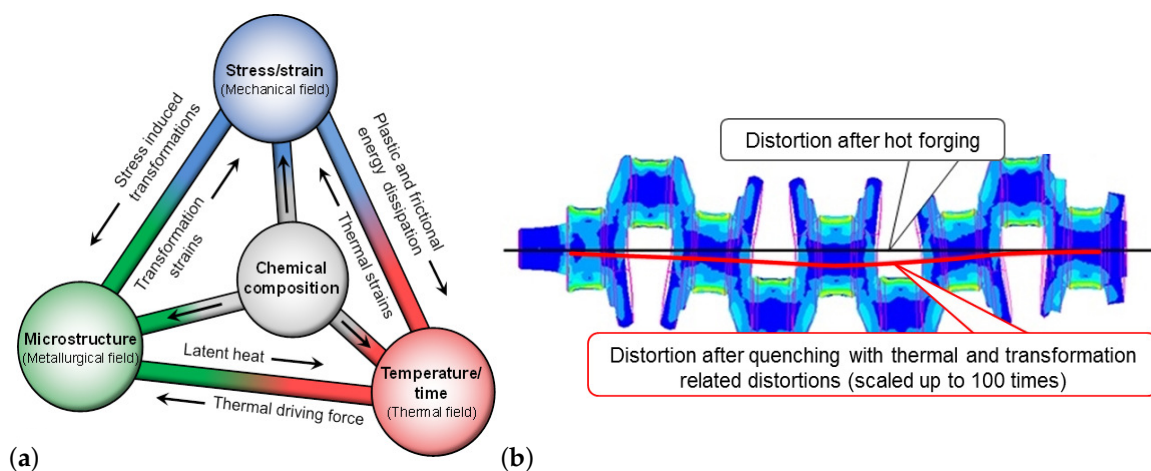

Figure 1. (**a**) Interrelated thermo-mechanical-metallurgical material phenomena during thermo-mechanical processing of steel [8] and (**b**) distortion of an exemplarily forged part after heat treatment [9].

In general, according to [10], there are three different types of residual stresses which are explained in the following. Residual stresses of the first type refer to the complete component and can be defined as macroscopic. The difference between the mean stress of a grain and the macroscopic residual stress is regarded as residual stress of the second type, while the location-dependent deviations of the stresses within the grain from the sum of first and second type are called residual stresses of the third type, cf. [11–13].

The resulting mechanical properties of steels strongly depend on the physical processes, e.g., hardening and phase transformations, occurring during the material production and the manufacturing. Thus, in numerical modeling, the consideration of these aspects is crucial to obtain good reliability and prediction.

The diffusionless phase transformation, i.e., austenite to martensite, is a key aspect in the improvement of metal properties. In [14], as well as [15], macroscopic constitutive models for its consideration in a large strain plasticity setting is proposed. In the investigations carried out by [16,17], a macroscopic approach to simulate the aforementioned transformation process as well as the effect of transformation induced plasticity (TRIP) is introduced. In their research [8,18] are contributing to the Finite Element (FE) supported calculation of phase transformations regarding the anisotropic transformation strains during martensitic transformation by using a user-defined FE code based on the mathematical network of [19,20]. In general, for fully coupled thermo-mechanical-metallurgical process simulations on the macroscale following [21,22], FE codes based on the theory of additive

strain decomposition (ASD) are used. The total strain increment is decomposed into an elastic-, plastic-, thermal-, transformation- and a TRIP-strain component, respectively. In the work of [16], first steps towards a multiscale approach within a homogenization scheme are presented.

Based on these investigations in [23,24], the multiscale approach is extended to further phases, e.g., bainite, pearlite, and steel types, e.g., low alloy ones. All the previously mentioned works use the FE Method for the numerical simulation. A further technique for the description of the physical aspects is the Multi-Phase-Field (MPF) model, which is introduced in [25–27]. This model is based on the consistent formulation of diffusional and surface driven phase transitions and allows the calculation of interfacial tension, multiphase thermodynamics and elastic stress balance in multiple junctions between an arbitrary number of grains and phases. Numerous publications have picked up on this model for the description of a variety of multi-physics effects, starting from single grain simulation up to the evolution of dendrites. In context of this publication, it is referred to [28–30], wherein the transformation process inside metals during production and manufacturing are taken into account. An implementation of the MPF model is available in the software library OpenPhase, which is distributed under the GNU General Public License (GPL) and is free of charge; see [31]. Actual studies concerning martensite transformation using the phase-field theory can be found in [32–35].

In the scope of this work, an insight into the experimental and numerical analysis of the material behavior in thermo-mechanical forming processes as well as simulation approaches of residual stresses on different scales is provided. The paper is organized as follows: Section 2 describes the experimental treatment of the forming process of cylindrical specimen. The macroscopic FE simulation model is presented in Section 3. In Section 4, the macroscopic results of the experiment and the simulation are compared. A numerical process of the investigation of residual stresses on mesoscale and microscale is described in Section 5. Section 6 provides a conclusion.

2. Experimental Procedure

To investigate the development of residual stresses, the steel alloy 1.3505 (DIN designation according to [36]: 100Cr6) was thermo-mechanically processed by upsetting at 1000 °C with subsequent cooling. Following [20], cylindrical specimen with eccentric holes were used, as inhomogeneous residual stresses are expected over the circumference of the specimen. The specimen were prepared with six thermocouples as shown in Figure 2. Three thermocouples are located on the thin-walled side (positions are indicated as TC1 to TC3) and three thermocouples on the thick-walled side (TC4 to TC6), respectively. The prepared specimens were placed in a thermobox together with the tools as shown in Figure 3a which enables the upsetting test to be carried out isothermally.
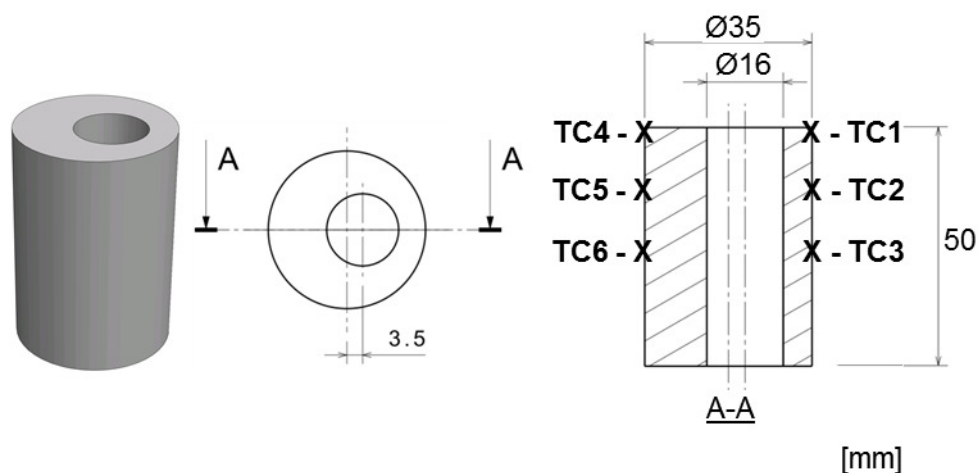

Figure 2. Shape of the investigated specimen with dimensions in mm and location of the thermocouples on the specimen surface.
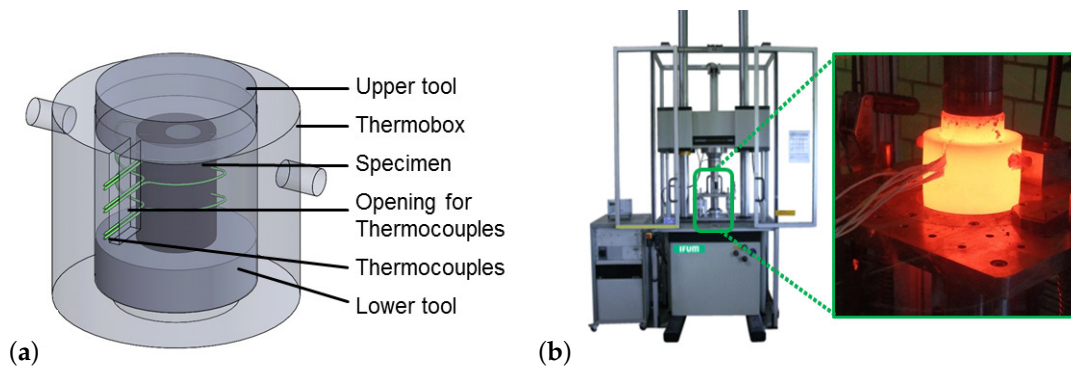
Figure 3. (**a**) Schematic representation of the specimen prepared with thermocouples in the thermobox and (**b**) servohydraulic forming simulator of the company Instron with the glowing thermobox inserted.

The temperature time profile is shown schematically in Figure 4, illustrating the process procedure. The prepared specimens were heated to 1000 °C inside the thermobox including the upper and lower tools in an oven, which has been manufactured by Nabertherm GmbH. After the desired temperature of 1000 °C had been reached, a ten-minute holding time followed to achieve a homogeneous austenitic structure. Since the austenitization conditions have an influence on the grain size and the grain size in turn has an impact on the phase-transformation behavior, all experiments were carried out using the identical austenitization conditions (1000 °C, 10 min), which result in a grain with the ASTM grain size number 8 according to [37,38]. Subsequently, the thermobox including the tools and the specimen was transferred to the servohydraulic forming simulator. The specimens were upset from initial height of 50 mm to a final height of about 28 mm at a punch speed of 200 mm/s. In the next step, the specimen were removed from the thermobox and either quenched in cold water or cooled down to room temperature in still air. During the entire process chain, the temperature was measured via the thermocouples of type K (NiCr-Ni, manufacturer Günther GmbH). The bare thermocouple wires with a diameter of 0.5 mm have been welded directly onto the specimen. Using the measuring amplifier MX1609 (max. 600 Hz, manufacturer HBM GmbH), the temperatures have been successfully recorded at a sampling rate of 100 Hz for quenching in water and 5 Hz for air cooling.

Due to the two cooling media of water and air, different temperature time profiles and consequently different transformation kinematics (see Figure 4) have been observed in the steel alloys. During rapid cooling in water, a diffusionless transformation occurs, where austenite is transformed into the martensitic body-centered tetragonal (bct) lattice structure. When cooled by air, a body-centered cubic (bcc) lattice with a ferritic, pearlitic, or bainitic microstructure depending on the cooling path is formed, as a consequence of a diffusion-controlled transformation. As a result, various residual stress conditions and distortions are expected in the differently cooled specimen.
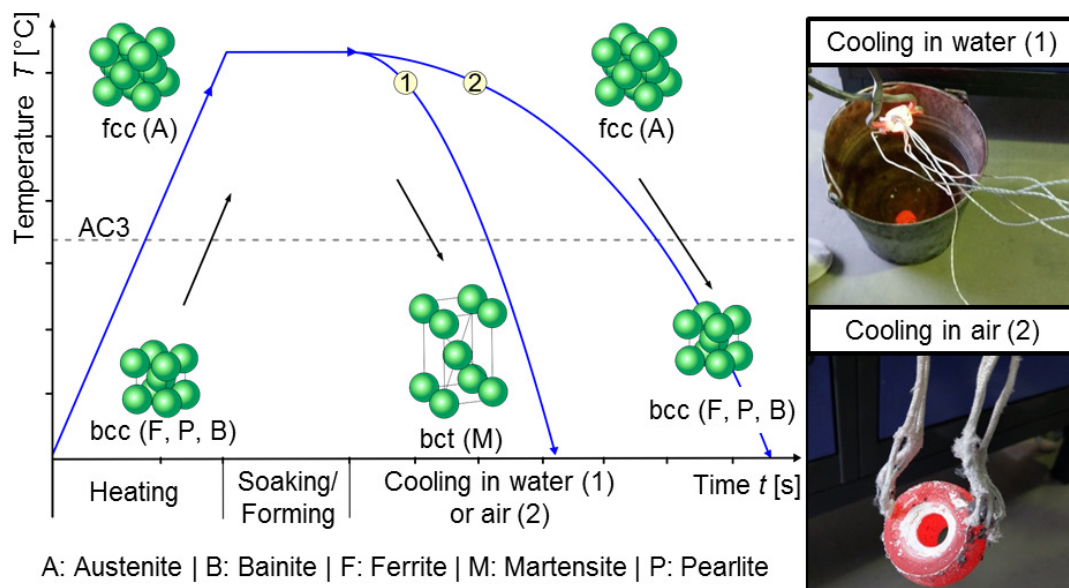
Figure 4. Principle representation of the temperature time profile in the experiments with respect to phase-transformation kinematics.

After thermo-mechanical processing, both axial and tangential residual stresses were measured on the surface of the specimen at the mid-height. The surface of the specimen at the locus of the measuring point was electrolytically polished, in order to avoid the influence of scale layers on the measurement. Residual stresses were determined by X-ray diffraction employing the $\sin^2 \Psi$ method in accordance with the corresponding DIN norm [39]. For this purpose a Ψ-diffractometer type XSTRESS X3000 G2 from Stresstech GmbH using Cr Kff radiation was applied. The measuring spot was determined by a 2 mm point collimator, whereas the tilting area of Ψ was varied with a total of nine tilt positions. The evaluation of the residual stress measurements was carried out with the software XTronic (Stresstech GmbH). The X-ray elasticity constants ($s_1 = -1.27 \cdot 10^{-6} \, \mathrm{mm^2/N}$, $\frac{1}{2} s_2 = 5.81 \cdot 10^{-6} \, \mathrm{mm^2/N}$) and the reference values for the unstressed material ($d_{211} = 1.1703 \, \text{Å}$, $2\theta_{Cr} = 156.084°$) were taken from the tabular data collection of [40]. These data of X-ray elasticity constants were calculated as mean values from the so-called Voigt [41] and Reuß [42] approaches for the pure alpha iron lattice.

Furthermore, flow curves for the 1.3505 steel alloy were determined by means of standard cylindrical upsetting tests, in order to characterize the flow behavior in the hot forming process. The characterization tests were carried out on the servohydraulic forming simulator Gleeble 3800-GTC at IFUM for the relevant temperatures 900 °C, 1000 °C, 1100 °C and 1200 °C with the equivalent plastic strain rate $1 \, \mathrm{s^{-1}}$. In addition, the tests were carried out at a temperature of 1000 °C with the equivalent plastic strain rates $10 \, \mathrm{s^{-1}}$ and $50 \, \mathrm{s^{-1}}$. Temperature control by means of thermocouples allowed the test to be carried out isothermally.

3. Numerical Procedure for Macroscopic FE Simulation

The previously described thermo-mechanical cylinder upsetting tests were numerically modeled with the commercial FE software Simufact.forming 14 using MSC.marc solver. A time-temperature-transformation (ttt) diagram, accounting for polymorphic behavior of the investigated steel alloy 1.3505 was implemented in the FE-software; see [43]. To simulate the viscoplastic material flow during hot forming, the flow stress of the material was implemented in the model as a function of equivalent plastic strain ε_{eq}, equivalent plastic strain rate $\dot{\varepsilon}_{eq}$ and temperature T. To calibrate this multidimensional function, flow curves were experimentally determined as described

in Section 3. The results of the characterization experiments as well as the calibration of the regression coefficients are presented in Section 4.

To numerically reproduce the thermo-mechanical forming process including the cooling step, phase-specific material data, such as flow curves, coefficients of TRIP, and specific heat capacity are required. In most cases, it is difficult to generate experimental material data for pure structural phases [44]. For this reason, material data has been generated with the thermodynamic simulation software [45] as an initial estimation. With help of this software, it is possible to generate mechanical and thermal material data by means of thermodynamic calculation approaches from [46,47] based on the chemical composition of steel alloys. The calculated phase-dependent flow curves for austenite and martensite are exemplarily shown in Figure 5. In addition, more detailed information on the calculated phase-specific material data is presented in tabular form in the Appendix A. The respective chemical composition employed for the material data computation is shown in Table 1 and was taken from the inspection certificate of the investigated steel grade from the steel supplier. With this data in hand, simulations of the thermo-mechanical process are performed, in the manner described below.
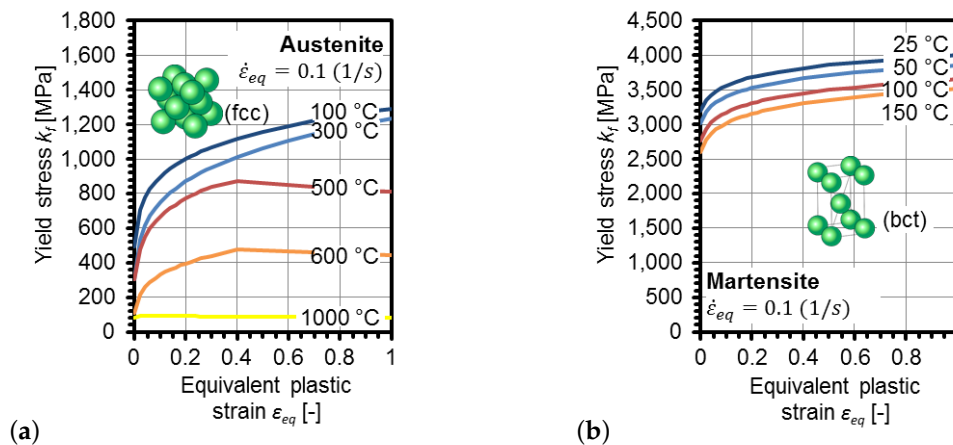
Figure 5. Phase-specific flow curves for steel alloy 1.3505 for (**a**) austenite and (**b**) martensite.

Table 1. Chemical composition of the investigated steel alloy 1.3505 used for material data generation with JMatPro.

Chemical Composition [wt%]	C	Si	Mn	P	S	Cr	Mo	Fe
1.3505 (DIN 100Cr6)	0.99	0.25	0.35	0.025	0.015	1.475	0.1	balance

As mentioned before, it can be assumed that almost no residual stresses from previous process steps are present in the material due to austenitization. For this reason, it was sufficient to start the process simulation under the initial condition of a 100% austenitic structure and a thermally expanded workpiece at 1000 °C. Furthermore, the symmetry of the specimen was exploited by using a half model for the simulations.

Figure 6 shows the FE model in Simufact.forming and the considered boundary conditions. The tools were treated as heat-conducting rigid bodies, as it is usual in hot forming, and provided with a mesh of 1 mm edge length. For the tools made of 2.4668 (DIN NiCr19NbMo), constant values for specific heat capacity $c_p = 435$ J/kgK and heat conductibility $\lambda = 11.4$ W/mK were taken from the supplier's data [48]. For the workpiece, an adaptive hex-mesh with a minimal element edge length of 0.5 mm has been employed, which was determined within a mesh sensitivity analysis. In total, 56,500 hex elements were used for the workpiece, whereby each tool was modeled with 24,000 hex elements.

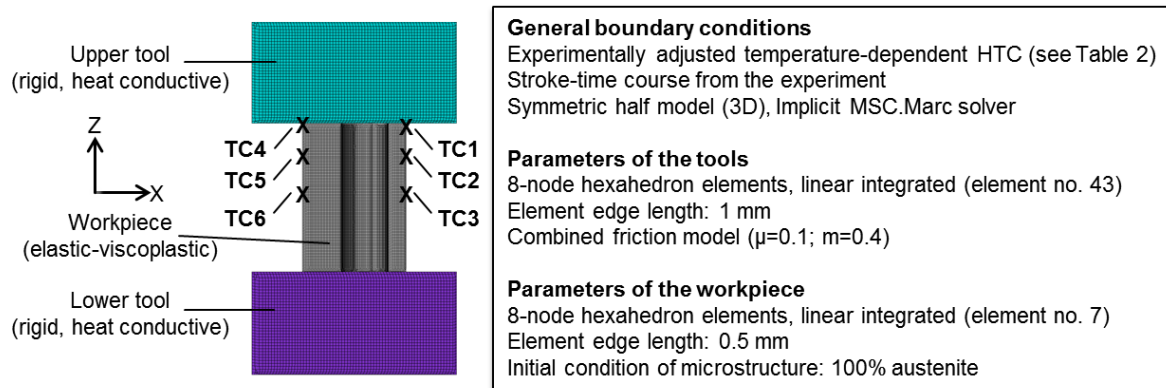**Figure 6.** Schematics of the considered FE model with the positions of thermocouples (TC1 to TC6) and the boundary conditions.

4. Comparison of Experimental and Numerical Results for Macroscopic Model Validation

The determined flow curves at the investigated temperatures and equivalent plastic strain rates are shown in Figure 7a. The parameters (A, m_1, m_2, m_3, m_4) of the following approach according to [49], cf. Equation (1) and Table 2, were determined using the method of the smallest error squares to continuously describe the flow stress k_f as a function of equivalent plastic strain ε_{eq}, equivalent plastic strain rate $\dot{\varepsilon}_{eq}$ and temperature T,

$$k_f = A\, e^{(m_1 T)} \varepsilon_{eq}^{m_2} e^{m_4/\varepsilon_{eq}} \dot{\varepsilon}_{eq}^{m_3} . \tag{1}$$

Table 2. Parameters determined for the calculation of the flow stress k_f of the considered steel alloy 1.3505 according to [49].

A in MPa	m_1	m_2	m_3	m_4
2208	−0.003068	−0.179	0.1695	−0.04383

As shown in Figure 7b, the plasticity model for the hot forming process step was validated by force-displacement-curves from experiment and simulation. The temperature time profiles are subject to several influencing parameters. Simufact.forming therefore considers thermal data, such as specific heat capacity, heat conduction, and latent heat, which were calculated with JMatPro; see Appendix A. Since the modeling of the correct temperature profile is particularly important for the simulation of the phase transformations and finally the residual stresses, heat transfer coefficients (HTC) were also optimized. The HTC between steel and the cooling media air or water were determined in iterative numerical optimizations to accurately represent the cooling of the specimen in the simulation. Thus, they can be regarded as empirically fitted for the experiment under consideration. Initial values for temperature-dependent HTC for air and water were calculated based on literature data [50]. In an iterative optimization procedure, the HTCs were adjusted using the experimental data from thermocouple 3 (TC). The calculated HTC values are presented in Table 3. Afterwards, the temperature profiles of the different measuring points from experiment and simulation, based on the calculated HTC data, were compared. As shown exemplarily for TC 2 in Figure 8, the temperature profiles could be successfully simulated.

(**a**)

(**b**)
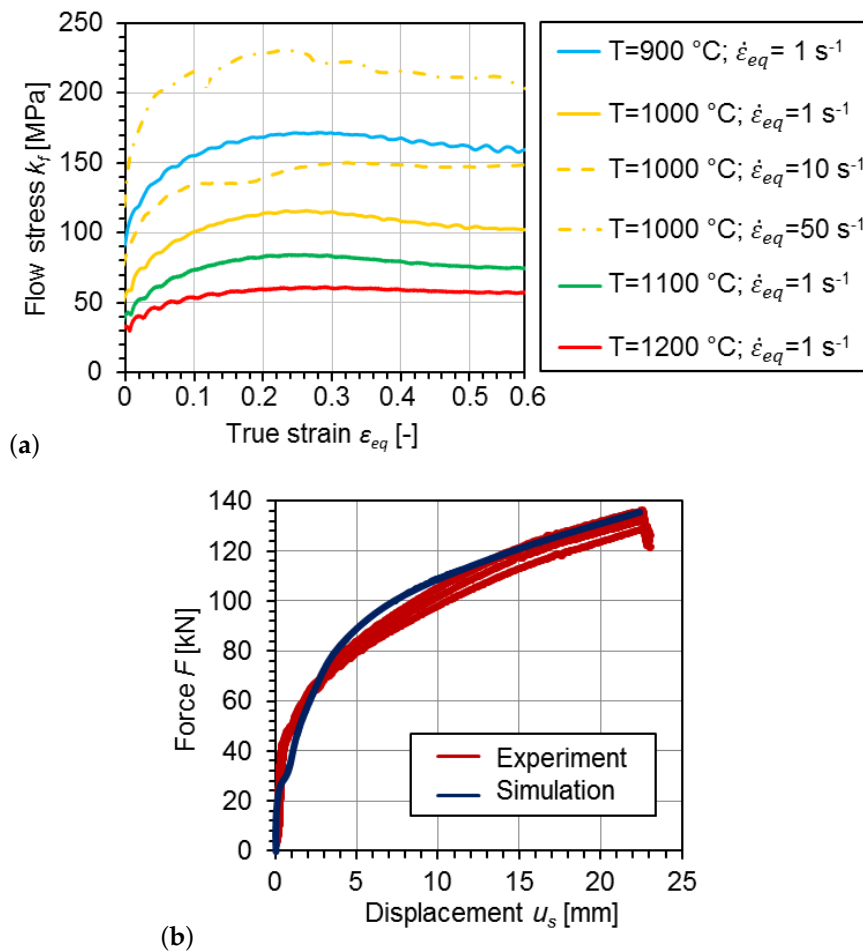
Figure 7. (**a**) Determined flow curves for hot forming applications from servohydraulic forming simulator Gleeble 3800-GTC and (**b**) comparison of force-displacement-curves from experiments and simulations.
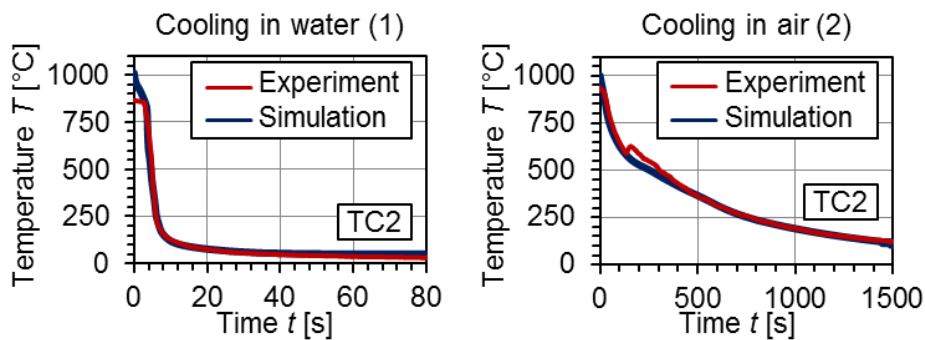
Figure 8. Time-temperature-profiles from experiments and optimized simulations from TC 2.

The upset specimen from experiment were optically investigated to evaluate the resulting distortions from thermo-mechanical processing. The CAD-model of a specimen from experiment could be created by 3D scanning, applying the optical measurement system ATOS (GOM GmbH). Subsequently, the dimensional accuracy of the FE simulation was visualized using the software INSPECT (GOM GmbH). Figure 9 shows the geometry of the specimen from experiment. The contour plot of the deviation e on this surface indicates the three-dimensional distance in perpendicular direction to the surface of the geometry from the simulation.

Table 3. Numerically identified heat transfer coefficients between specimen and the cooling media air or water for material 1.3505.

Temperature in °C	HTC in W/m²K	
	Cooling Medium	
	Water (1)	Air (2)
70	2510.62	18.45
120	5290.64	18.65
170	10,514.1	18.72
220	10,514.1	18.84
270	11,636.3	25.63
320	8615.18	30.48
370	7635.76	22.12
420	7175.43	20.95
470	7103.66	18.11
520	5806.81	8.97
570	5080.56	26.59
620	7174.87	40.25
670	6175.83	50.62
720	6427.27	64.30
770	2928.02	88.79
820	970.37	112.55
870	793.31	89.47
920	630.00	61.31
970	810.68	55.28
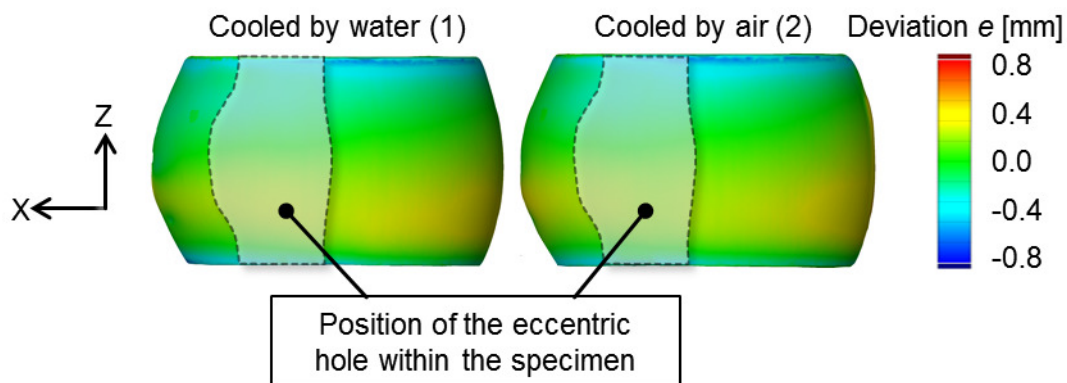
Figure 9. Visualization of the dimensional accuracy between the simulated geometry and the real specimen, analyzed with the optical measurement system ATOS (GOM GmbH).

A deviation of 0 mm shows a perfect match between the geometry from the simulation and the experiment. The algebraic sign of the deviation value indicates if the corresponding area of the geometry from the simulation lies outside (positive sign) or inside (negative sign) the workpiece shape from the experiment. As can be seen in Figure 9, a maximum deviation of about $e = 0.4$ mm was determined.

The hardness of the material depends on the resulting phase structure which is related to the transformation mechanisms and the cooling time. Hence, the hardness measurement according to Vickers [51] provides an important reference point for assessing the quality of the microstructure transformation simulation. For these metallographic investigations, the specimen were cut into two parts by wire erosion as shown in Figure 10a. Afterwards, Vickers hardness measurements were carried out at six measuring points (MP1 to MP6). The comparison of hardness values from experiment and simulation shows that the evolution of microstructure during cooling could be predicted well by the numerical model, c.f. Figure 10b. In addition, the corresponding microstructure in MP2 of the differently treated specimen is shown exemplarily in Figure 10c. As expected, a martensitic structure

was formed by cooling in water, recognizable by the needle-shaped structure. A fine striped pearlitic structure was found on the specimen cooled by air, respectively. Consequently, the higher hardness values on the martensitic specimen after cooling in water and the lower hardness values on the pearlitic specimen after cooling in air are plausible.
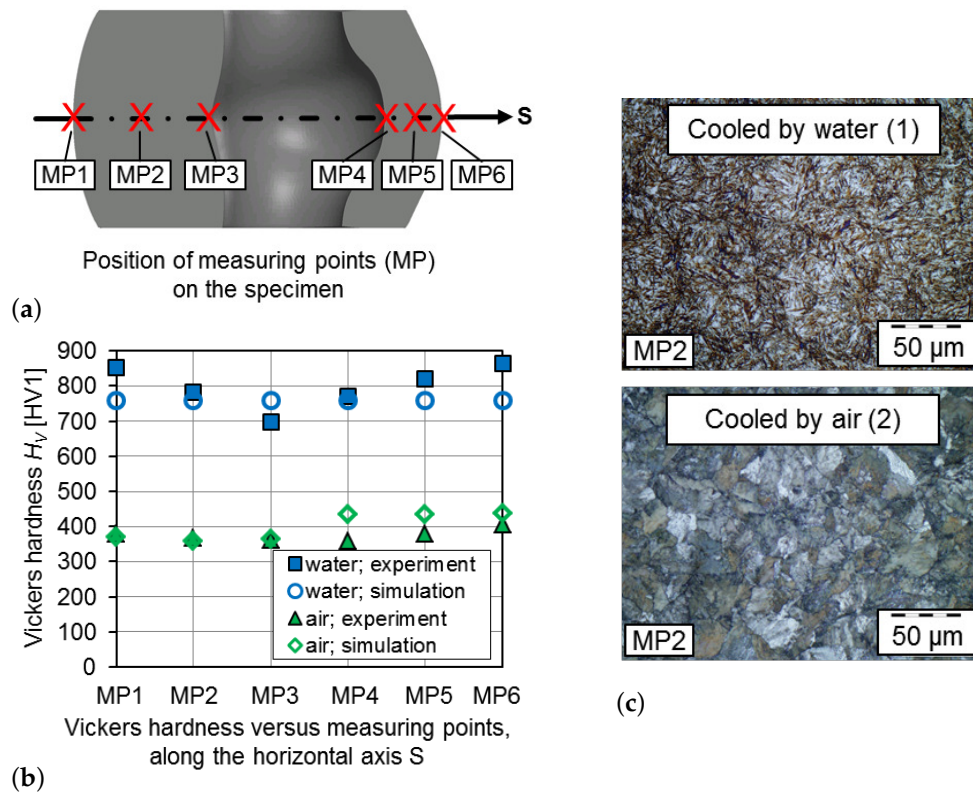
Figure 10. (**a**) Positions of the measuring points (MP1 to MP6) along the horizontal axis S on the differently treated specimen, (**b**) results of Vickers hardness and (**c**) resulting microstructure after thermo-mechanical processing at MP2.

Figure 11 presents a comparison of simulation results with XRD residual stress measurements. Here, the arithmetic mean with the absolute deviations of the tangential σ_t as well as the axial σ_{ax} residual stresses on the specimen surface at the locations of MP1 and MP6 on the mid-height are considered. In the X-ray measurements, negative stresses between 50 MPa and 100 MPa were detected on the specimen cooled by air. The simulation also predicts low residual stress values in the range of -5 MPa to -7 MPa for this cooling route. These minor residual stresses can be attributed to the diffusion-controlled phase transformation during cooling in air. For the specimen cooled by water, different values were measured on the surface of the thick-walled specimen side (MP1) and the thin-walled specimen side (MP6). The axial residual stress at MP1 is $\sigma_{ax} = 307$ MPa and at MP6 $\sigma_{ax} = 100$ MPa respectively. In the tangential direction, residual stresses of $\sigma_t = 183$ MPa at MP1 and $\sigma_t = 138$ MPa at MP6 were measured. As expected, the geometry of the specimen with an eccentric hole causes an inhomogeneous residual stress distribution.
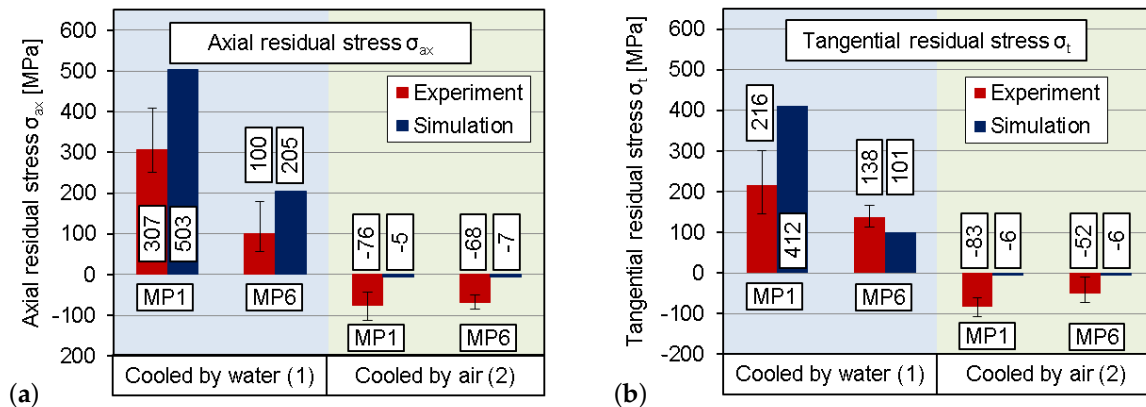
Figure 11. Arising residual stresses in (**a**) axial σ_{ax} and (**b**) tangential σ_t direction on the surface of differently treated specimen at MP1 (thick-walled side) and MP6 (thin-walled side).

The developed FE model was able to predict the occurrence of tension or compression stresses for all the considered cases. In addition, the qualitative amount, especially the differences of the residual stresses between MP1 and MP6, could be predicted. However, the simulation overestimates the axial residual stresses at MP1 and MP6 as well as the tangential residual stress at MP1. The tangential residual stress at MP6 could be predicted with a good accuracy.

As shown in Figure 1, thermal, metallurgical and mechanical interactions in the material must be taken into account for the numerical description of the residual stresses. Due to these numerous interacting parameters, an exact calculation of the residual stresses is challenging. In particular, the TRIP strains take a significant impact on the resulting residual stresses [8]. Therefore, the calculation of TRIP strains used in the simulation model by MSC.Marc solver could be extended. On the one hand, the load-dependent and reversible back-stress effects resulting from a stress relief during martensitic transformation can be included in the simulations. On the other hand, the work in [18] shows that the TRIP behavior has different effects on the deformation at tensile and compressive loads. For a further improvement of the model, these influences could be considered separately. With the simulation model presented in this paper, it was possible to make an appropriate qualitative prediction of the macroscopic residual stresses resulting from different cooling routes.

However, it is assumed that local stress gradients have also been developed, for example due to dislocations within the grains resulting from plastic deformations or phase transformations at the microstructural scale. These local deviations represented by residual stresses of second and third type can have a particular influence on the macroscopic stresses. Therefore, in future work in-depth numerical investigations on the microscale are to be performed in order to further analyze the interactions of the residual stresses of first, second, and third type and to quantitatively improve the prediction accuracy of the residual stresses; see Section 5.

5. Numerical Investigation of Residual Stresses on Micro- and Mesoscale

In the previous section, the thermo-mechanical process was numerically modeled on a macroscopic scale, taking into account the boundary conditions from the experiment. Since complex thermal, metallurgical, and mechanical interactions occur on the microstructural level of the material, a consideration of the residual stress development on these minor scales is motivated. By investigating the residual stress development on the microscale, further knowledge about the influence of the residual stresses of the second and third type on the measurable macroscopic residual stresses can be obtained, in order to further improve the prediction accuracy of the model. Therefore, based on data obtained from the experimental and simulative investigations of the previous sections, a numerical model is developed in the following, which accounts for the phase transformation from austenite to martensite (A-M) during rapid cooling and investigates the resulting residual stress distribution on a mesoscopic level. Herein, the mesoscopic level describes a polycrystal with multiple grains. Therefore,

MPF simulations in combination with FE simulation are used and applied to the investigated material 1.3505. At this point, the complex process of phase transformation is simulated with a rather simple approach, which shall be understood as a first attempt towards a realistic model.

Since the A-M phase transformation changes the crystalline structure inside the grain but not the intergranular boundary, the latter is assumed to be fixed throughout the simulation. Starting from the microscopic scale on the level of one grain, the evolution of different martensite variants is simulated. The homogenized eigenstrain of the resulting laminate structures is then transferred to the mesoscopic level and thereby accounts for the strain jump during the evolution of martensite. A polycrystalline structure consisting of multiple grains is considered, which is obtained from MPF simulation applying normal grain growth. In this first attempt, the A-M transformation is considered by prescribing a homogenized eigenstrain to each austenitic grain. Using an energy minimization principle, the final eigenstrain distribution on the mesoscale is obtained from the MPF model. Since only elastic strains are considered, an FE model is used to incorporate the elasto-plastic behavior of the material. In a two-scale FE simulation associated with the experimental setting in Section 2, the eigenstrain distribution of the mesoscale is applied and the elasto-plastic response is computed. At the end, the resulting distribution of residual stresses is obtained. The following section elucidates the details on the briefly explained procedure above, which is additionally illustrated in Figure 12.

5.1. Multi-Phase-Field Simulation

The used MPF model, introduced in [25], can consider an arbitrary number of phases in the simulation, which differ from each other by e.g., orientation. An implementation is available as open-source software [31]. The underlying governing equation is represented by the free energy density F in a domain Ω as

$$F = \int_\Omega f^{\text{intf}} + f^{\text{chem}} + f^{\text{elast}} \, \mathrm{d}\Omega, \tag{2}$$

where f^{intf} represents the interfacial energy, f^{chem} the chemical energy and f^{elast} the elastic energy density, respectively. They can be calculated by

$$
\begin{aligned}
f^{\text{intf}} &= \sum_{\alpha,\beta=1,....,N,\alpha\neq\beta} \frac{4\sigma_{\alpha\beta}}{\eta_{\alpha\beta}} \left[-\frac{\eta_{\alpha\beta}^2}{\pi^2} \nabla\phi_\alpha \cdot \nabla\phi_\beta + \phi_\alpha\phi_\beta \right], \\
f^{\text{chem}} &= \sum_{\alpha=1,....,N} h(\phi_\alpha) f_\alpha(c_\alpha^i) + \tilde{\mu}^i (c^i - \sum_{\alpha=1,....,N} \phi_\alpha c_\alpha^i), \\
f^{\text{elast}} &= \frac{1}{2} \left[\sum_{\alpha=1,....,N} h(\phi_\alpha)(\varepsilon_\alpha - \varepsilon_\alpha^* - c_\alpha^i \varepsilon_\alpha^i) : \mathbb{C}_\alpha : (\varepsilon_\alpha - \varepsilon_\alpha^* - c_\alpha^j \varepsilon_\alpha^j) \right],
\end{aligned}
\tag{3}
$$

where $\phi_{[\bullet]}$ denotes the phase-field parameter of phase-field $[\bullet]$.

The evolution of the phase-field parameter is controlled by the diffusion equation reading

$$\dot{\phi}_\alpha = \sum_{\beta=1,....,N} \frac{\pi^2 \mu_{\alpha\beta}}{8\eta N} \left(\frac{\partial F}{\partial \phi_\beta} - \frac{\partial F}{\partial \phi_\alpha} \right). \tag{4}$$

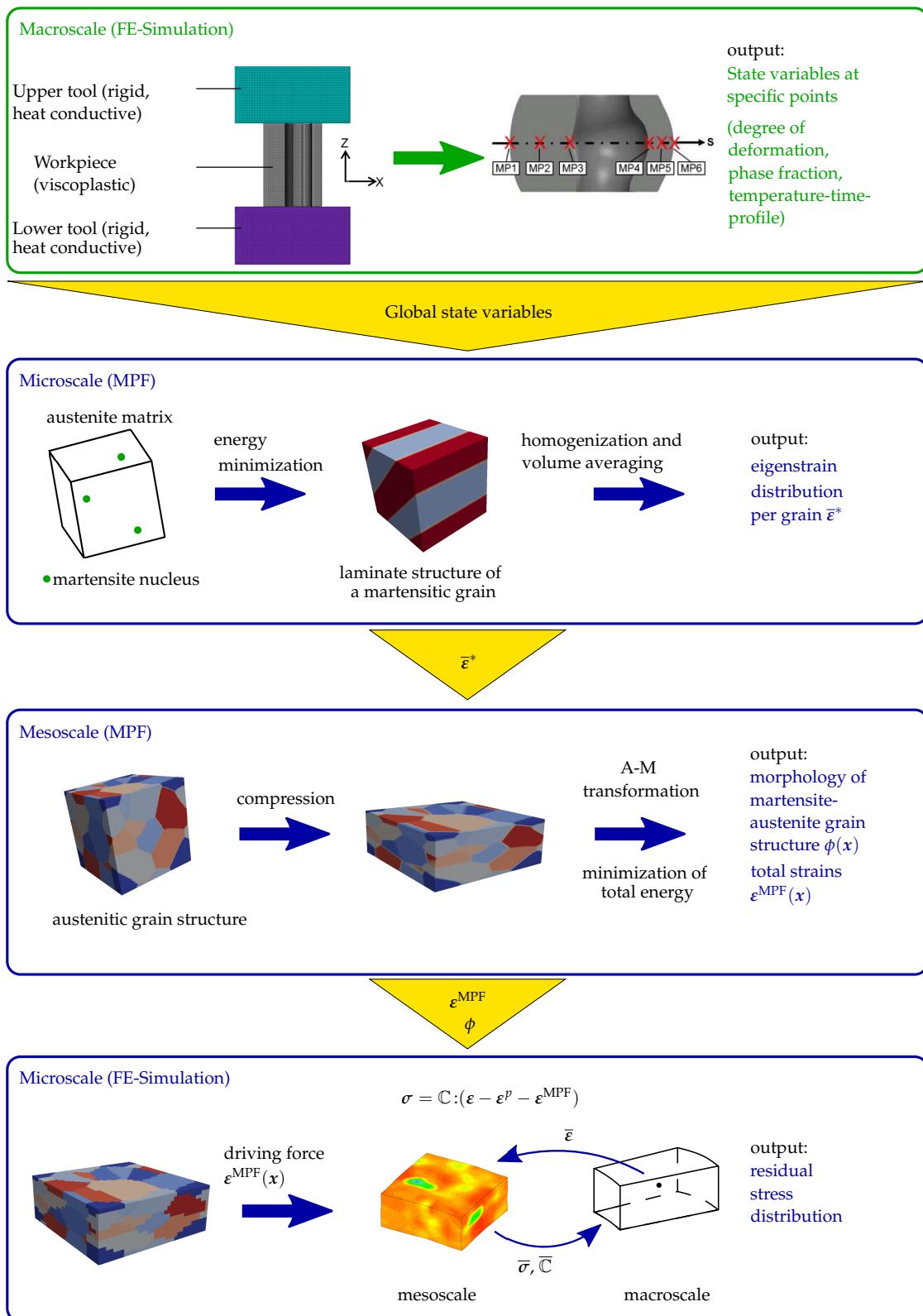**Figure 12.** Simulation procedure of macro-, meso-, and microscale using Multi-Phase-Field Model and FE Simulation. Note that ε, ε^p, ε^{MPF}, $\overline{\varepsilon}^*$ denotes the total strains, the plastic strains, the mesoscopic strain distribution resulting from the A-M phase transformation and the eigenstrain distribution per grain, respectively.

Further quantities used in Equations (3) and (4) are described in Table 4.

Table 4. Quantities governing the energy densities in Equations (2) and (3).

i, j	components
α, β	identifier of phase-fields
N	total number of phase-fields
$\sigma_{\alpha\beta}$	energy of the interface between phase-fields α and β
$\eta_{\alpha\beta}$	interface width between phase-fields α and β
$f_\alpha(c_\alpha^i)$	chemical potential for phase-field α
c_α^i	concentration of component i in phase-field α
$\tilde{\mu}^i$	generalized chemical potential or diffusion potential as Lagrange multiplier for satisfying the balance of mass for each component $(c^i = \sum_{\alpha=1,\ldots,N} \phi_\alpha c_\alpha^i)$
ε_α	total strain of phase-field α
ε_α^*	eigenstrain of phase-field α
ε_α^i	strain of component i in phase-field α
$\mathbb{C}_\alpha$	elasticity tensor of phase-field α
$h(\phi_\alpha)$	polynomial function fulfilling $h(1) = 1$ and $h(0) = 0$ with $h(\phi_\alpha) = \phi_\alpha$
$\mu_{\alpha\beta}$	effective interfacial mobility between phase-fields α and β

5.1.1. Homogenization of Eigenstrains on Microscale

To describe the transformation from austenite to martensite (A-M), different martensitic variants must be taken into account. This diffusionless transformation is caused by fast cooling of heated austenite in water as described in Section 2. In this context, the three so-called Bain-groups are considered (see [52]) which describe possible types of tetragonal transformation of the cubic unit cell, cf. Figure 13a. Shearing and rotation has to be considered additionally but will be neglected due to simplicity. In a first step, in order to simulate the martensite microstructure evolution inside one grain, austenite with three martensitic nuclei is considered in a MPF simulation, where each nucleus represents a possible martensite variant. A transversally isotropic eigenstrain state given by ε_I^*, ε_{II}^* or ε_{III}^* with

$$
\begin{aligned}
\operatorname{diag} \varepsilon_I^* &= \begin{bmatrix} -0.2 & 0.12 & 0.12 \end{bmatrix}, \\
\operatorname{diag} \varepsilon_{II}^* &= \begin{bmatrix} 0.12 & -0.2 & 0.12 \end{bmatrix}, \\
\operatorname{diag} \varepsilon_{III}^* &= \begin{bmatrix} 0.12 & 0.12 & -0.2 \end{bmatrix},
\end{aligned}
\tag{5}
$$

represents the volume change during tetragonal transformation, I, II and III, respectively. Although these tensors do not fall into the range of small strains anymore, the linear approach is suitable due to high temperatures during application of the transformation scheme. This results in three possible laminate microstructures consisting of two variants, (i.e., I, II or II, III or I, III), following the principle of minimizing the total energy in the system; see Figure 13b.

To obtain the mechanical energy and the mechanical driving force, a homogenization scheme is applied to calculate the individual phase-field strain distribution, which is presented in [53–55] and applied to OpenPhase in [56]. Therefore, a partial rank-one homogenization is used, which satisfies the static equilibrium and the strains compatibility condition at the interfaces.

The strain jump between phase-fields α and β for linear elastic materials in a small strain framework is given by

$$
\varepsilon_\beta - \varepsilon_\alpha = \operatorname{sym}(\boldsymbol{a} \otimes \boldsymbol{n}),
\tag{6}
$$

cf. [54], where $\boldsymbol{n}$ is the normal vector of the interface and $\boldsymbol{a}$ characterizes the jump of the displacement gradient

$$
\boldsymbol{a} = -\left[\boldsymbol{n} \cdot [\phi_\beta \mathbb{C}_\alpha + \phi_\alpha \mathbb{C}_\beta] \cdot \boldsymbol{n}\right]^{-1} \cdot \left[\mathbb{C}_\beta : [\varepsilon_\beta - \varepsilon_\beta^*] - \mathbb{C}_\alpha : [\varepsilon_\alpha - \varepsilon_\alpha^*]\right] \cdot \boldsymbol{n}.
\tag{7}
$$
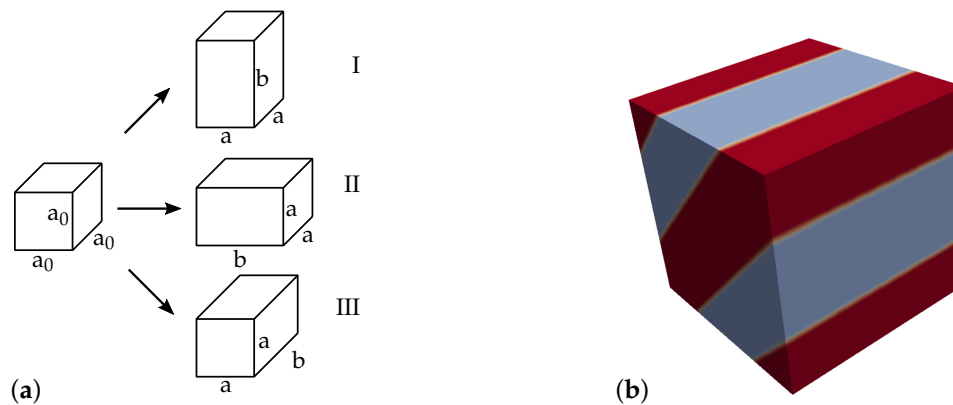
Figure 13. (**a**) Variants of martensite, cf. [52], with a_0 as edge length of an austenitic unit cell and a, b as edge length of a tetragonally transformed martensitic unit cell and (**b**) laminate consisting of two variants of martensite.

All other parameters are explained in Table 4. The effective (homogenized) eigenstrain tensor representing the internal laminate structure of one martensite grain can be computed by volume averaging, whereas the laminate consists of equal amounts of the two variants. This describes the transition between the microscopic single grain level and the mesoscopic polycrystal. Hence, the three effective eigenstrain tensors, which describe the eigenstrains homogenized over the domain of one martensitic grain on the mesoscale, read

$$
\begin{aligned}
\operatorname{diag} \bar{\varepsilon}_{\mathrm{II,III}}^{*} &= \begin{bmatrix} 0.12 & -0.04 & -0.04 \end{bmatrix}, \\
\operatorname{diag} \bar{\varepsilon}_{\mathrm{I,III}}^{*} &= \begin{bmatrix} -0.04 & 0.12 & -0.04 \end{bmatrix}, \\
\operatorname{diag} \bar{\varepsilon}_{\mathrm{I,II}}^{*} &= \begin{bmatrix} -0.04 & -0.04 & 0.12 \end{bmatrix}.
\end{aligned}
\tag{8}
$$

5.1.2. Mesoscopic Phase Transformation

For the description of phase transformation on the mesoscale, a polycrystalline structure with multiple grains is considered. At the beginning of the simulation, all grains are considered to be austenite, whereas the grains differ by the orientation of the crystallographic lattice. This granular structure is obtained from a MPF simulation involving normal grain growth (see Equation (3)1–2) where a cubic grid with 121 points in each direction is defined. It consists of one austenitic phase with 24 randomly placed nuclei with different orientations. The material properties for the considered material 1.3505 for nuclei and matrix are given by an isotropic elasticity tensor, which is derived by interpolation of Young's modulus E and Poisson's ratio ν generated using JMatPro, cf. Appendix A, for austenite and martensite at the martensitic start temperature taken as 375 °C, i.e.,

$$
\begin{aligned}
E^{\mathrm{A}} &= 169{,}819\,\mathrm{MPa}, & \nu^{\mathrm{A}} &= 0.3122, \\
E^{\mathrm{M}} &= 185{,}606\,\mathrm{MPa}, & \nu^{\mathrm{M}} &= 0.30332.
\end{aligned}
$$

In the MPF simulation, the 24 grains start to grow from the nuclei and the matrix vanishes. The simulation is continued until the matrix has completely vanished. In order to account for the retained austenite, three grains of the evolved granular structure are considered to be austenite in the subsequent calculation of austenite-to-martensite (A-M) transformation. The amount of austenite in the mesostructure was observed in a conceptional study related to the experiments; see Section 3. Thus, the other 21 grains are considered for the simulation of martensitic phase transformation. Next, the deformation of the structure during compression must be accounted for. By assuming a linear mapping of the geometry of the cubic grid under the assumption that no volume change occurs, the bulging of the cylindrical specimen, resulting in a reduction in height by 50%, is described on the

mesostructure. Subsequently, the linear mapping is performed with a factor of 0.5 for the reduction of height and the respective elongation in the two remaining directions considering volume preservation. The deformed grid is now defined by 61 grid points in height and 171 in width and length, respectively; see Figure 14b.

(a)　　　　　　　　　　　　(b)　　　　　　　　　　　　(c)
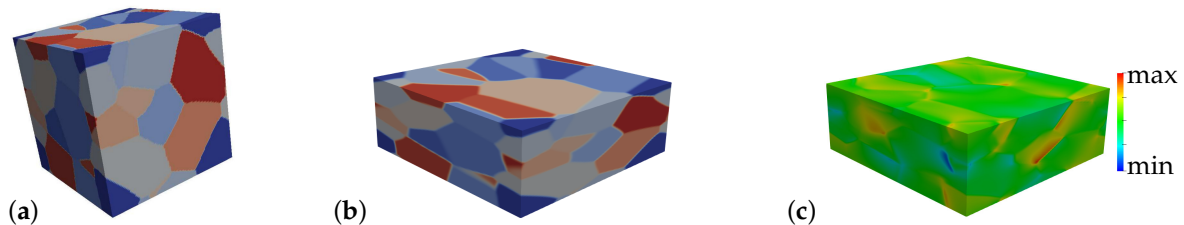
Figure 14. (**a**) Austenitic grain growth with different orientations for the grains, which are indicated by coloring, (**b**) austenitic cube with 50 % deformation regarding height and (**c**) first component of mesoscopic strain distribution from the MPF model $\varepsilon^{\mathrm{MPF}}$.11.

Hence, the structure represents a polycrystal consisting yet of austenitic grains. The A-M transformation is modeled by applying one homogenized eigenstrain state for each grain. Since it is not known which of the three possible homogenized eigenstrain states is dominant in each grain, a simple minimization scheme based on the total elastic energy f^{elast} is used to identify a possible set of eigenstrain states. Therefore, the set of all eigenstrain states is defined by

$$V = \{\varepsilon_1^*, ..., \varepsilon_{21}^*\} \quad \text{for} \quad \varepsilon_i^* \in \{\bar{\varepsilon}_{\mathrm{II,III}}^*, \bar{\varepsilon}_{\mathrm{I,III}}^*, \bar{\varepsilon}_{\mathrm{I,II}}^*\}. \tag{9}$$

Initially, a random effective eigenstrain tensor ε_i^* is defined for each of the 21 grains. Next, it is checked whether one of the other two effective eigenstrain states in $\{\bar{\varepsilon}_{\mathrm{II,III}}^*, \bar{\varepsilon}_{\mathrm{I,III}}^*, \bar{\varepsilon}_{\mathrm{I,II}}^*\}$ leads to a smaller energy level, whereas only one grain can be changed at a time. This iterative procedure is repeated several times until no change of eigenstrain state leads to a smaller energy level. The procedure can be described by the minimization scheme

$$\tilde{V} = \arg\left[\min_V[f^{\mathrm{elast}}(V)]\right], \tag{10}$$

whereas $\tilde{V}$ defines the set of eigenstrain states in the grains which leads to a minimization of the elastic energy. According to the application of this final set of eigenstrains $\tilde{V}$, a mesoscopic strain distribution $\varepsilon^{\mathrm{MPF}}(x)$ results from the A-M phase transformation. Figure 14c shows the strain distribution on the mesoscopic structure, which serves as input, i.e., driving force, for the computation of residual stresses in the following section.

5.2. FE Simulation of Mesoscopic Residual Stress

For the mesoscopic modeling of the stress distribution because of the austenite-martensite transformation a two-scale FE simulation is considered. In particular, the calculation of the elasto-plastic mechanical behavior due to the evolving eigenstrains should be enabled. Based on that, the total strains $\varepsilon^{\mathrm{MPF}}(x)$ resulting from the MPF model for the optimal set of applied eigenstrains (see Equation (10)) are taken into account as the driving force in the FE simulation. The mechanical behavior of each phase is represented by the application of an elasto-plastic material law with a von Mises yield criterion with exponential hardening; see e.g., [57]. The set of necessary equations for the formulation is given in Table 5.

Table 5. Set of equations for von Mises plasticity with exponential hardening considering additive split of strain tensor ε into elastic ε^e and plastic part ε^p following [58].

kinematic	$\varepsilon^e = \varepsilon - \varepsilon^p$, $\mathrm{dev}\,\varepsilon^e = \varepsilon^e - \frac{1}{3}\,\mathrm{tr}\,\varepsilon^e\,\boldsymbol{I}$
stresses	$\sigma = \kappa\,\mathrm{tr}(\varepsilon^e)\,\boldsymbol{I} + 2\,\mu\,\mathrm{dev}\,\varepsilon^e$
conjugated internal variable	$\beta = \partial_{\tilde{\alpha}}\,\psi = -(y_\infty - y_0)(\exp(-\delta\,\tilde{\alpha}) - 1) + h\,\tilde{\alpha}$
reduced internal dissipation	$\mathcal{D}_{int} = \sigma : \dot{\varepsilon}^p - \beta\,\dot{\tilde{\alpha}} \geq 0$
yield criterion	$\Phi = \|\mathrm{dev}\,\sigma\| - \sqrt{\frac{2}{3}}[y_0 + \beta] \leq 0$
flow rule	$\dot{\varepsilon}^p = \lambda\boldsymbol{n}$, $\boldsymbol{n} = \frac{\mathrm{dev}\,\sigma}{\|\mathrm{dev}\,\sigma\|}$
evolution of internal variables	$\dot{\tilde{\alpha}} = -\lambda\partial_\beta\,\Phi = \lambda\sqrt{\frac{2}{3}}$
Kuhn-Tucker conditions	$\lambda \geq 0$, $\Phi \leq 0$, $\lambda\Phi = 0$

The material parameters describing the mechanical behavior in the elastic domain, i.e., bulk modulus κ and Lamé constant μ, are recalculated from the values used in Section 5.1.2. The plastic behavior of the material model is fitted to the flow curves generated using JMatPro for both phases at 375 °C, cf. Figure 5a,b. The resulting material parameters are listed in Table 6.

Table 6. Material parameters for austenite and martensite for 1.3505 at temperature $T = 375$ °C.

	κ in MPa	μ in MPa	y_0 in MPa	y_∞ in MPa	δ —	h in MPa
austenite	150,709.09	64,707.74	300.0	685.0	23.5	500.0
martensite	157,282.56	71,205.08	2200.0	2675.0	19.0	550.0

To incorporate the strain distribution $\varepsilon^{\mathrm{MPF}}(x)$ resulting from the austenite-to-martensite (A-M) transformation evaluated using the MPF model into the FE simulation, the strain field on element level is incrementally modified over pseudo-time t, i.e.,

$$\varepsilon(u, x, t^{n+1}) \Leftarrow \varepsilon(u, x, t^n) - \varepsilon^{\mathrm{MPF}}(x, t^{n+1}). \tag{11}$$

Therefore, the last and actual time step is indicated by t^n and t^{n+1}, respectively. For the strain distribution $\varepsilon^{\mathrm{MPF}}$, which is computed for each grid point in the MPF model, a one on one mapping from grid point to FE is considered, i.e., $\varepsilon^{\mathrm{MPF}}$ is constant over each element domain. To enable a simplified mapping, a voxel-like representation of the structure is achieved using hexahedral FEs with 20 nodes and quadratic shape functions. The same mapping is applied for the phase-field parameter to reconstruct the mesoscopic grain structure in the FE model. In order to reduce the computational costs, the grid of the MPF model from Section 5.1 is coarsed to a voxel-based representation of $35 \times 35 \times 13$; see Figure 15.
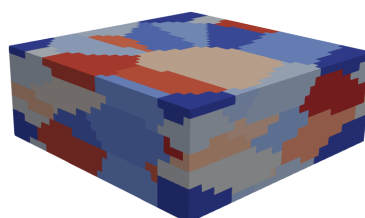
Figure 15. Reconstruction of the periodic mesoscopic grain structure containing 21 martensitic grains and 3 austenitic grains: FE model with 15,925 cubic elements with 136,107 nodes.

Based on the afore mentioned discretization of a granular mesoscopic structure, a two-scale boundary value problem is solved; see Figure 16. On the macroscale, a cylindrical section motivated by the specimen used in the experimental setup shown in Section 3, is considered. Therefore, the boundary conditions are enforced as shown in Figure 16 due to the assumption of an axis symmetry, where r, φ and z denote the radial and tangential and height component, respectively. On the mesoscale, periodic boundary conditions are applied. The classical micro-macro transition approach, also known as FE^2-method, solves a mesoscopic boundary value problem at each macroscopic FE integration point. The macroscopic quantities are computed by suitable averages and the quantities associated with the macroscale are denoted by an overline. For further details see e.g., [59,60].
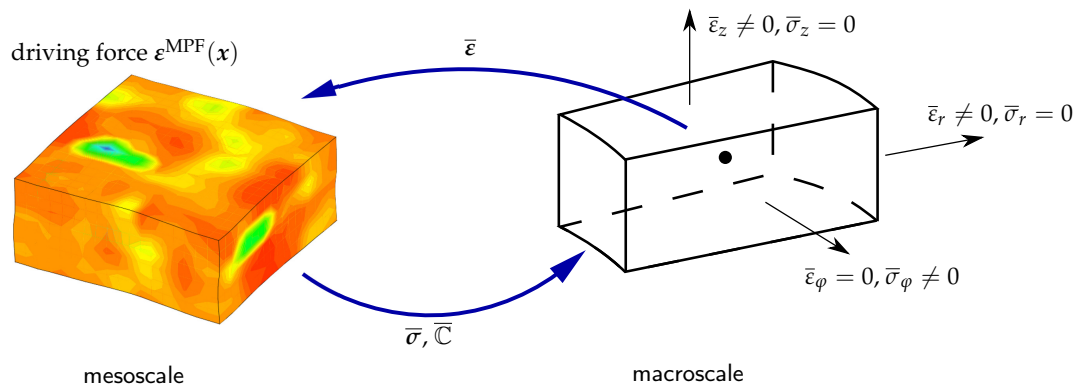
Figure 16. Two-scale boundary value problem for the incorporation of the strains $\varepsilon^{\mathrm{MPF}}(x)$ in the FE model.

In Figure 17a–c, the resulting mesoscopic stress distributions due to the application of the A-M transformation are shown. Since the equilibrium state on the macroscale is considered in the quasi-static simulation and no external forces are applied to the cylindrical specimen, the resultant stress distribution can be interpreted as residual stress, rather than mechanical stress. Stresses tangential to the outer surface of the cylindrical specimen (see Figure 17b) are in the main focus of further investigation. These quantities are most relevant with respect to the durability of the manufactured component. Additionally, it has to be noticed that the radial stresses vanish macroscopically, since $\bar{\sigma}_r = 0.875 \cdot 10^{-12} \approx 0$ holds, which is enforced by the boundary conditions, which state that $\bar{\sigma}_r = \bar{\sigma}_z = 0$ and $\bar{\sigma}_\varphi \neq 0$ as shown in Figure 16. As stated earlier, such stress states can be interpreted as residual stress due to the chosen boundary conditions.
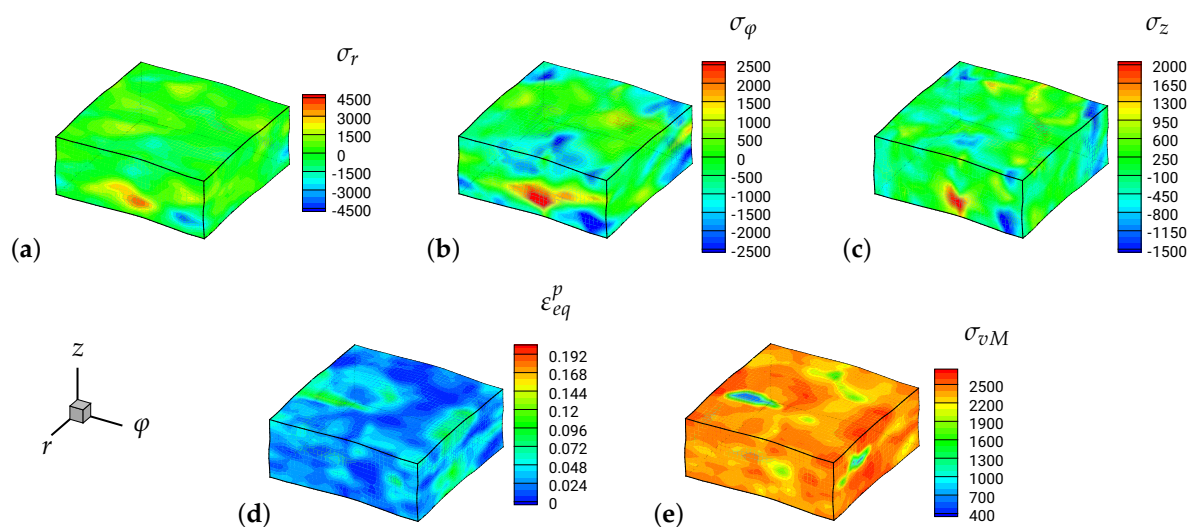
Figure 17. (**a**) Radial stresses σ_r in MPa, (**b**) tangential stresses σ_φ in MPa, (**c**) axial stresses σ_z in MPa, (**d**) equivalent plastic strains and (**e**) von Mises stress in MPa.

6. Conclusion and Outlook

In this work, the material behavior of the steel alloy 1.3505 during the thermo-mechanical forming process was investigated by experiments and simulation approaches on different scales regarding microstructural transformation behavior and the resulting residual stresses. Upsetting tests of cylindrical specimen with eccentric holes were performed at 1000 °C with subsequent cooling in the media water or air to achieve different inhomogeneous residual stress states. Following this, the properties of the specimen were experimentally analyzed. Using an optical 3D scanning method of the experimental specimen, the dimensional accuracy of the geometries from the simulations could be evaluated. In addition, the resulting microstructure of the material was examined by light microscopy and the hardness was measured using the Vickers testing method. In addition, the residual stresses at certain points on the surface of the specimen were measured by X-ray diffraction. A macroscopic simulation model was created with the commercial software Simufact.forming using experimental determined ttt-diagrams and flow curves. Furthermore, HTC were optimized for the considered process. The macroscopic FE model was able to qualitatively predict the residual stresses evolving from the considered thermo-mechanical forming process.

For the description of the evolution of mechanical fields due to microstructural effects on the lower scales, a multiscale approach was proposed based on a MPF model and a two-scale FE simulation. This method is used to describe the residual stresses on the microscale resulting from the austenite-to-martensite transformation.

In a future step, by analyzing the interactions of the residual stresses from micro- and macro-simulations, the prediction accuracy of the arising residual stresses in thermo-mechanical forming processes shall be further improved. From that, the influence of the residual stresses of second and third type on the measurable residual stresses of first type can be derived. Therefore, the improvement of the cooling process in the experiment and the validation of the macroscopic simulation to achieve a stable and useful residual stress state can be enabled.

Appendix A

Appendix A.1. Temperature-Dependent Properties of Material 1.3505

Table A1. Material parameters for austenite and martensite for 1.3505.

1.3505—Specific Heat Capacity c_p [J/(kg K)]					
Temperature T [$^\circ$ C]	Austenite	Ferrite	Pearlite	Bainite	Martensite
25	4.54×10^2	4.46×10^2	4.75×10^2	4.75×10^2	4.49×10^2
100	4.78×10^2	4.77×10^2	5.02×10^2	5.02×10^2	4.81×10^2
200	5.02×10^2	5.17×10^2	5.37×10^2	5.37×10^2	5.23×10^2
300	5.22×10^2	5.61×10^2	5.75×10^2	5.75×10^2	5.69×10^2
400	5.40×10^2	6.16×10^2	6.22×10^2	6.22×10^2	6.25×10^2
500	5.57×10^2	6.86×10^2	6.82×10^2	6.82×10^2	6.95×10^2
600	5.73×10^2	7.83×10^2	7.77×10^2	7.77×10^2	7.93×10^2
700	5.89×10^2	9.38×10^2	9.15×10^2	9.15×10^2	9.46×10^2
800	6.04×10^2	8.26×10^2	8.41×10^2	8.41×10^2	8.36×10^2
950	6.29×10^2	7.22×10^2	7.80×10^2	7.80×10^2	7.33×10^2

1.3505—Thermal Conductivity λ [J/(m s K)]					
Temperature T [$^\circ$ C]	Austenite	Ferrite	Pearlite	Bainite	Martensite
25	1.72×10^1	3.37×10^1	3.95×10^1	3.95×10^1	3.36×10^1
100	1.81×10^1	3.58×10^1	3.92×10^1	3.92×10^1	3.56×10^1
200	1.93×10^1	3.75×10^1	3.82×10^1	3.82×10^1	3.73×10^1
300	2.05×10^1	3.79×10^1	3.68×10^1	3.68×10^1	3.77×10^1
400	2.17×10^1	3.71×10^1	3.51×10^1	3.51×10^1	3.70×10^1
500	2.29×10^1	3.56×10^1	3.33×10^1	3.33×10^1	3.54×10^1
600	2.41×10^1	3.36×10^1	3.15×10^1	3.15×10^1	3.35×10^1
700	2.53×10^1	3.19×10^1	2.99×10^1	2.99×10^1	3.17×10^1
800	2.65×10^1	3.06×10^1	2.88×10^1	2.88×10^1	3.04×10^1
950	2.83×10^1	2.99×10^1	2.84×10^1	2.84×10^1	2.98×10^1

1.3505—Coefficient of Thermal Expansion α_{th} [1/K]					
Temperature T [$^\circ$ C]	Austenite	Ferrite	Pearlite	Bainite	Martensite
25	2.33×10^{-5}	1.24×10^{-5}	1.16×10^{-5}	1.16×10^{-5}	1.22×10^{-5}
100	2.32×10^{-5}	1.26×10^{-5}	1.18×10^{-5}	1.18×10^{-5}	1.24×10^{-5}
200	2.32×10^{-5}	1.30×10^{-5}	1.22×10^{-5}	1.22×10^{-5}	1.28×10^{-5}
300	2.32×10^{-5}	1.33×10^{-5}	1.26×10^{-5}	1.26×10^{-5}	1.31×10^{-5}
400	2.32×10^{-5}	1.37×10^{-5}	1.30×10^{-5}	1.30×10^{-5}	1.35×10^{-5}
500	2.32×10^{-5}	1.41×10^{-5}	1.34×10^{-5}	1.34×10^{-5}	1.38×10^{-5}
600	2.31×10^{-5}	1.44×10^{-5}	1.38×10^{-5}	1.38×10^{-5}	1.42×10^{-5}
700	2.31×10^{-5}	1.48×10^{-5}	1.43×10^{-5}	1.43×10^{-5}	1.45×10^{-5}
800	2.31×10^{-5}	1.52×10^{-5}	1.48×10^{-5}	1.48×10^{-5}	1.49×10^{-5}
950	2.31×10^{-5}	1.57×10^{-5}	1.58×10^{-5}	1.58×10^{-5}	1.54×10^{-5}

1.3505—Density ρ [kg/m^3]				
Temperature T [$^\circ$C]	Austenite	Ferrite	Pearlite	Bainite	Martensite
25	7.97×10^3	7.83×10^3	7.80×10^3	7.80×10^3	7.71×10^3
100	7.93×10^3	7.81×10^3	7.78×10^3	7.83×10^3	7.69×10^3
200	7.88×10^3	7.78×10^3	7.75×10^3	7.75×10^3	7.66×10^3
300	7.82×10^3	7.74×10^3	7.72×10^3	7.72×10^3	7.63×10^3
400	7.77×10^3	7.71×10^3	7.69×10^3	7.69×10^3	7.59×10^3
500	7.72×10^3	7.67×10^3	7.65×10^3	7.65×10^3	7.56×10^3
600	7.67×10^3	7.64×10^3	7.62×10^3	7.62×10^3	7.52×10^3
700	7.61×10^3	7.60×10^3	7.58×10^3	7.58×10^3	7.49×10^3
800	7.65×10^3	7.56×10^3	7.54×10^3	7.54×10^3	7.45×10^3
950	7.43×10^3	7.50×10^3	7.47×10^3	7.47×10^3	7.39×10^3

1.3505—Youngs's Modulus E [Pa]				
Temperature T [$^\circ$C]	Austenite	Ferrite	Pearlite	Bainite	Martensite
25	2.01×10^{11}	2.10×10^{11}	2.10×10^{11}	2.10×10^{11}	2.10×10^{11}
100	1.95×10^{11}	2.07×10^{11}	2.07×10^{11}	2.07×10^{11}	2.07×10^{11}
200	1.86×10^{11}	2.01×10^{11}	2.01×10^{11}	2.01×10^{11}	2.01×10^{11}
300	1.77×10^{11}	1.93×10^{11}	1.94×10^{11}	1.94×10^{11}	1.93×10^{11}
400	1.68×10^{11}	1.83×10^{11}	1.84×10^{11}	1.84×10^{11}	1.83×10^{11}
500	1.59×10^{11}	1.71×10^{11}	1.73×10^{11}	1.73×10^{11}	1.71×10^{11}
600	1.50×10^{11}	1.58×10^{11}	1.61×10^{11}	1.61×10^{11}	1.58×10^{11}
700	1.41×10^{11}	1.43×10^{11}	1.48×10^{11}	1.48×10^{11}	1.44×10^{11}
800	1.31×10^{11}	1.28×10^{11}	1.33×10^{11}	1.33×10^{11}	1.29×10^{11}
950	1.17×10^{11}	1.04×10^{11}	1.11×10^{11}	1.11×10^{11}	1.05×10^{11}

1.3505—Possion's Ration $\Delta d/d$ [-]				
Temperature T [$^\circ$C]	Austenite	Ferrite	Pearlite	Bainite	Martensite
25	2.9×10^{-1}	2.90×10^{-1}	2.87×10^{-1}	2.87×10^{-1}	2.90×10^{-1}
100	2.96×10^{-1}	2.93×10^{-1}	2.90×10^{-1}	2.90×10^{-1}	2.92×10^{-1}
200	3.02×10^{-1}	2.97×10^{-1}	2.93×10^{-1}	2.93×10^{-1}	2.96×10^{-1}
300	3.07×10^{-1}	3.01×10^{-1}	2.96×10^{-1}	2.96×10^{-1}	3.00×10^{-1}
400	3.13×10^{-1}	3.05×10^{-1}	3.00×10^{-1}	3.00×10^{-1}	3.04×10^{-1}
500	3.19×10^{-1}	3.09×10^{-1}	3.03×10^{-1}	3.03×10^{-1}	3.08×10^{-1}
600	3.24×10^{-1}	3.13×10^{-1}	3.06×10^{-1}	3.06×10^{-1}	3.12×10^{-1}
700	3.30×10^{-1}	3.17×10^{-1}	3.10×10^{-1}	3.10×10^{-1}	3.16×10^{-1}
800	3.36×10^{-1}	3.21×10^{-1}	3.13×10^{-1}	3.13×10^{-1}	3.20×10^{-1}
950	3.44×10^{-1}	3.27×10^{-1}	3.19×10^{-1}	3.19×10^{-1}	3.26×10^{-1}

1.3505—TRIP-Coefficient C_{TP} [mm^2/N]				
Temperature T [$^\circ$C]	Ferrite	Pearlite	Bainite	Martensite
25	9.04×10^{-5}	5.36×10^{-5}	5.36×10^{-5}	8.37×10^{-5}
100	9.87×10^{-5}	5.59×10^{-5}	5.59×10^{-5}	9.19×10^{-5}
200	1.01×10^{-4}	5.33×10^{-5}	5.33×10^{-5}	9.49×10^{-5}

1.3505—Latent Heat c_L [J/kg]				
Temperature T [$^\circ$C]	Ferrite	Pearlite	Bainite	Martensite
25	1.51×10^5	1.62×10^5	1.62×10^5	8.25×10^4
100	1.51×10^5	1.61×10^5	1.61×10^5	8.26×10^4
200	1.50×10^5	1.58×10^5	1.58×10^5	8.15×10^4
300	1.47×10^5	1.53×10^5	1.53×10^5	7.81×10^4
400	1.40×10^5	1.47×10^5	1.47×10^5	7.16×10^4
500	1.29×10^5	1.36×10^5	1.36×10^5	6.06×10^4
600	1.11×10^5	1.20×10^5	1.20×10^5	4.30×10^4
700	7.36×10^4	9.44×10^4	9.44×10^4	1.48×10^4
800	-	6.06×10^4	6.06×10^4	-2.04×10^4
950	-	3.40×10^4	3.40×10^4	-4.34×10^4

1.3505—Hardness H [N/m^2]	
Cooling time from 800 $^\circ$C to 500 $^\circ$C [s]	H
30,000.00	6.91×10^8
10,000.00	7.22×10^8
6000.00	7.35×10^8
4285.71	7.44×10^8
3333.33	7.51×10^8
1500.00	1.29×10^9
750.00	2.45×10^9
500.00	2.57×10^9
375.00	2.59×10^9
300.00	2.60×10^9
100.00	2.61×10^9
60.00	2.61×10^9
42.86	2.61×10^9
33.33	2.61×10^9
15.00	2.61×10^9
7.50	2.61×10^9
5.00	2.61×10^9
3.75	2.61×10^9
3.00	2.61×10^9

1.3505—Austenite
Equivalent plastic strain ε_{eq} [−], Yield stress k_f [Pa], Temperature T [° C], Strain rate $\dot{\varepsilon} = 0.001\,\mathrm{s}^{-1}$

ε_{eq}	$k_f(T=25)$	$k_f(T=250)$	$k_f(T=500)$	$k_f(T=750)$	$k_f(T=1000)$
0.00	4.03×10^8	2.59×10^8	2.52×10^8	8.65×10^7	4.05×10^7
0.02	6.21×10^8	4.88×10^8	4.23×10^8	1.23×10^8	4.75×10^7
0.06	7.49×10^8	6.24×10^8	4.69×10^8	1.23×10^8	4.75×10^7
0.08	7.88×10^8	6.67×10^8	4.69×10^8	1.23×10^8	4.74×10^7
0.12	8.46×10^8	7.32×10^8	4.67×10^8	1.23×10^8	4.73×10^7
0.14	8.70×10^8	7.59×10^8	4.66×10^8	1.23×10^8	4.72×10^7
0.18	9.10×10^8	8.04×10^8	4.63×10^8	1.22×10^8	4.69×10^7
0.20	9.27×10^8	8.24×10^8	4.61×10^8	1.21×10^8	4.66×10^7
0.24	9.58×10^8	8.60×10^8	4.56×10^8	1.20×10^8	4.62×10^7
0.26	9.72×10^8	8.76×10^8	4.54×10^8	1.19×10^8	4.60×10^7
0.30	9.97×10^8	9.05×10^8	4.49×10^8	1.18×10^8	4.54×10^7
0.40	1.05×10^9	9.68×10^8	4.39×10^8	1.15×10^8	4.43×10^7
0.60	1.13×10^9	1.06×10^9	4.21×10^8	1.11×10^8	4.26×10^7
0.70	1.16×10^9	1.10×10^9	4.15×10^8	1.09×10^8	4.20×10^7
0.90	1.21×10^9	1.17×10^9	4.03×10^8	1.06×10^8	4.08×10^7
1.00	1.24×10^9	1.20×10^9	3.99×10^8	1.05×10^8	4.03×10^7
2.00	1.40×10^9	1.41×10^9	3.68×10^8	9.67×10^7	3.72×10^7
3.00	1.51×10^9	1.55×10^9	3.50×10^8	9.21×10^7	3.54×10^7
4.00	1.59×10^9	1.66×10^9	3.38×10^8	8.90×10^7	3.42×10^7

1.3505—Bainite
Equivalent plastic strain ε_{eq} [−], Yield stress k_f [Pa], Temperature T [° C], Strain rate $\dot{\varepsilon} = 0.001\,\mathrm{s}^{-1}$

ε_{eq}	$k_f(T=25)$	$k_f(T=250)$	$k_f(T=500)$	$k_f(T=750)$	$k_f(T=1000)$
0.00	1.30×10^9	9.39×10^8	8.40×10^8	2.62×10^8	3.42×10^7
0.02	1.51×10^9	1.16×10^9	1.02×10^9	2.86×10^8	4.04×10^7
0.06	1.67×10^9	1.30×10^9	1.15×10^9	2.86×10^8	4.03×10^7
0.08	1.72×10^9	1.35×10^9	1.19×10^9	2.85×10^8	4.01×10^7
0.12	1.78×10^9	1.42×10^9	1.25×10^9	2.81×10^8	3.96×10^7
0.14	1.81×10^9	1.44×10^9	1.28×10^9	2.79×10^8	3.93×10^7
0.18	1.86×10^9	1.49×10^9	1.31×10^9	2.75×10^8	3.88×10^7
0.20	1.88×10^9	1.51×10^9	1.33×10^9	2.74×10^8	3.85×10^7
0.24	1.91×10^9	1.54×10^9	1.32×10^9	2.70×10^8	3.81×10^7
0.26	1.93×10^9	1.56×10^9	1.32×10^9	2.69×10^8	3.80×10^7
0.30	1.96×10^9	1.58×10^9	1.31×10^9	2.66×10^8	3.75×10^7
0.40	2.02×10^9	1.64×10^9	1.30×10^9	2.61×10^8	3.67×10^7
0.60	2.10×10^9	1.73×10^9	1.27×10^9	2.53×10^8	3.56×10^7
0.70	2.14×10^9	1.76×10^9	1.27×10^9	2.50×10^8	3.52×10^7
0.90	2.19×10^9	1.82×10^9	1.25×10^9	2.45×10^8	3.44×10^7
1.00	2.22×10^9	1.84×10^9	1.25×10^9	2.43×10^8	3.42×10^7
2.00	2.39×10^9	2.01×10^9	1.21×10^9	2.30×10^8	3.23×10^7
3.00	2.49×10^9	2.11×10^9	1.19×10^9	2.22×10^8	3.12×10^7
4.00	2.56×10^9	2.19×10^9	1.17×10^9	2.17×10^8	3.05×10^7

1.3505—Ferrite				
Equivalent plastic strain ε_{eq} [−], Yield stress k_f [Pa], Temperature T [° C], Strain rate $\dot{\varepsilon} = 0.001\,\mathrm{s}^{-1}$				
ε_{eq}	$k_f(T = 25)$	$k_f(T = 250)$	$k_f(T = 500)$	$k_f(T = 750)$	$k_f(T = 1000)$
0.00	1.39×10^8	6.74×10^7	4.94×10^7	4.69×10^7	7.30×10^6
0.02	2.41×10^8	1.37×10^8	1.00×10^8	7.00×10^7	9.68×10^6
0.06	2.86×10^8	1.65×10^8	1.20×10^8	6.99×10^7	9.66×10^6
0.08	2.99×10^8	1.73×10^8	1.26×10^8	6.96×10^7	9.62×10^6
0.12	3.19×10^8	1.86×10^8	1.35×10^8	6.87×10^7	9.51×10^6
0.14	3.27×10^8	1.91×10^8	1.38×10^8	6.82×10^7	9.44×10^6
0.18	3.40×10^8	1.99×10^8	1.44×10^8	6.73×10^7	9.31×10^6
0.20	3.46×10^8	2.03×10^8	1.47×10^8	6.69×10^7	9.25×10^6
0.24	3.56×10^8	2.10×10^8	1.51×10^8	6.61×10^7	9.14×10^6
0.26	3.60×10^8	2.13×10^8	1.53×10^8	6.58×10^7	9.10×10^6
0.30	3.69×10^8	2.18×10^8	1.57×10^8	6.51×10^7	9.01×10^6
0.40	3.86×10^8	2.29×10^8	1.64×10^8	6.38×10^7	8.82×10^6
0.60	4.12×10^8	2.46×10^8	1.76×10^8	6.19×10^7	8.55×10^6
0.70	4.22×10^8	2.52×10^8	1.80×10^8	6.11×10^7	8.45×10^6
0.90	4.39×10^8	2.63×10^8	1.88×10^8	5.99×10^7	8.29×10^6
1.00	4.47×10^8	2.68×10^8	1.91×10^8	5.94×10^7	8.22×10^6
2.00	4.99×10^8	3.02×10^8	2.15×10^8	5.62×10^7	7.77×10^6
3.00	5.32×10^8	3.24×10^8	2.30×10^8	5.43×10^7	7.52×10^6
4.00	5.57×10^8	3.41×10^8	2.41×10^8	5.31×10^7	7.34×10^6

1.3505—Martensite				
Equivalent plastic strain ε_{eq} [−], Yield stress k_f [Pa], Temperature T [° C], Strain rate $\dot{\varepsilon} = 0.001\,\mathrm{s}^{-1}$				
ε_{eq}	$k_f(T = 25)$	$k_f(T = 250)$	$k_f(T = 500)$	$k_f(T = 750)$	$k_f(T = 1000)$
0.00	2.94×10^9	2.19×10^9	7.80×10^8	5.64×10^7	7.35×10^6
0.02	3.10×10^9	2.38×10^9	8.15×10^8	7.02×10^7	9.75×10^6
0.06	3.24×10^9	2.54×10^9	8.13×10^8	7.00×10^7	9.72×10^6
0.08	3.29×10^9	2.59×10^9	8.10×10^8	6.98×10^7	9.69×10^6
0.12	3.35×10^9	2.67×10^9	8.00×10^8	6.89×10^7	9.57×10^6
0.14	3.38×10^9	2.70×10^9	7.95×10^8	6.84×10^7	9.50×10^6
0.18	3.43×10^9	2.75×10^9	7.84×10^8	6.75×10^7	9.37×10^6
0.20	3.45×10^9	2.78×10^9	7.79×10^8	6.71×10^7	9.31×10^6
0.24	3.48×10^9	2.81×10^9	7.70×10^8	6.63×10^7	9.21×10^6
0.26	3.50×10^9	2.83×10^9	7.66×10^8	6.60×10^7	9.15×10^6
0.30	3.53×10^9	2.86×10^9	7.59×10^8	6.53×10^7	9.07×10^6
0.40	3.58×10^9	2.93×10^9	7.43×10^8	6.40×10^7	8.88×10^6
0.60	3.67×10^9	3.02×10^9	7.21×10^8	6.20×10^7	8.61×10^6
0.70	3.70×10^9	3.06×10^9	7.12×10^8	6.12×10^7	8.51×10^6
0.90	3.75×10^9	3.12×10^9	6.98×10^8	6.01×10^7	8.34×10^6
1.00	3.78×10^9	3.15×10^9	6.92×10^8	5.95×10^7	8.27×10^6
2.00	3.93×10^9	3.33×10^9	6.55×10^8	5.63×10^7	7.82×10^6
3.00	4.02×10^9	3.44×10^9	6.33×10^8	5.44×10^7	7.56×10^6
4.00	4.09×10^9	3.52×10^9	6.18×10^8	5.32×10^7	7.39×10^6

1.3505—Pearlite				
Equivalent plastic strain ε_{eq} [−], Yield stress k_f [Pa], Temperature T [° C], Strain rate $\dot{\varepsilon} = 0.001\,\mathrm{s}^{-1}$				
ε_{eq}	$k_f(T=25)$	$k_f(T=250)$	$k_f(T=500)$	$k_f(T=750)$	$k_f(T=1000)$
0.00	5.58×10^8	3.76×10^8	3.33×10^8	2.50×10^8	3.42×10^7
0.02	7.47×10^8	5.47×10^8	4.72×10^8	2.74×10^8	4.04×10^7
0.06	8.59×10^8	6.42×10^8	5.51×10^8	2.74×10^8	4.03×10^7
0.08	8.92×10^8	6.70×10^8	5.74×10^8	2.74×10^8	4.01×10^7
0.12	9.42×10^8	7.12×10^8	6.09×10^8	2.73×10^8	3.96×10^7
0.14	9.61×10^8	7.29×10^8	6.23×10^8	2.72×10^8	3.93×10^7
0.18	9.94×10^8	7.58×10^8	6.47×10^8	2.71×10^8	3.88×10^7
0.20	1.01×10^9	7.70×10^8	6.57×10^8	2.71×10^8	3.85×10^7
0.24	1.03×10^9	7.92×10^8	6.75×10^8	2.70×10^8	3.81×10^7
0.26	1.04×10^9	8.01×10^8	6.83×10^8	2.69×10^8	3.80×10^7
0.30	1.07×10^9	8.19×10^8	6.98×10^8	2.66×10^8	3.75×10^7
0.40	1.11×10^9	8.56×10^8	7.28×10^8	2.61×10^8	3.67×10^7
0.60	1.17×10^9	9.11×10^8	7.73×10^8	2.53×10^8	3.56×10^7
0.70	1.20×10^9	9.32×10^8	7.91×10^8	2.50×10^8	3.52×10^7
0.90	1.24×10^9	9.69×10^8	8.21×10^8	2.45×10^8	3.44×10^7
1.00	1.25×10^9	9.85×10^8	8.34×10^8	2.43×10^8	3.42×10^7
2.00	1.38×10^9	1.10×10^9	8.62×10^8	2.30×10^8	3.23×10^7
3.00	1.46×10^9	1.17×10^9	8.40×10^8	2.22×10^8	3.12×10^7
4.00	1.52×10^9	1.22×10^9	8.25×10^8	2.17×10^8	3.05×10^7

References

1. Tekkaya, A.E.; Gerhardt, J.; Burgdorf, M. Residual Stresses in Cold-Formed Workpieces. *Manuf. Technol.* **1985**, *34*, 225–230. [CrossRef]
2. Mungi, M.P.; Rasane, S.D.; Dixit, P.M. Residual stresses in cold axisymmetric forging. *J. Mater. Process. Technol.* **2003**, *142*, 256–266. [CrossRef]
3. Von Mirbach, D. Hole-drolling method for residual stress measurement-consideration of elastic-plastic material properties. *Mater. Sci. Forum* **2014**, *768–769*, 174–181.
4. Behrens, B.A.; Schrödter, J. Numerical Simulation of Phase Transformation during the Hot Stamping Process. In Proceedings of the 5th International Conference on Thermal Process Modeling and Computer Simulation, Orlando, FL, USA, 16–18 June 2014; pp. 179–190.
5. Torres, M.A.S.; Voorwald, H.J.C. An evaluation of shot peening, residual stress and stress relaxation on the fatigue life of ASIS 4340 steel. *Int. J. Fatigue* **2002**, *24*, 877–886. [CrossRef]
6. Seidel, W. *Werkstofftechnik—Werkstoffe, Eigenspannungen, Prüfung, Anwendungen*, 7th ed.; Hanser: New York, NY, USA, 2007.
7. Behrens, B.A.; Bleck, W.; Bach, F.W.; Brinksmeier, E.; Fritsching, U.; Liewald, M.; Zoch, H.W. Resource-efficient process chains for high performance parts. *Key Eng. Mater.* **2012**, *504–506*, 151–156. [CrossRef]
8. Behrens, B.A.; Bouguecha, A.; Bonk, C.; Chugreev, A. Numerical and experimental investigations of the anisotropic transformation strains during martensitic transformation in a low alloy Cr-Mo steel 42CrMo4. *Procedia Eng.* **2017**, *207*, 1815–1820. [CrossRef]
9. Courtesy of DKK Co. 2018. Available online: https://www.denkikogyo.co.jp/en/business/hf/technology/simulation2.html (accessed on 1 August 2018).
10. Macherauch, E.; Wohlfahrt, H.; Wolfstied, U. Zur zweckmäßigen Definition von Eigenspannungen. *Härterei-Technische Mittelungen Z. Für Werkst. Wärmebehandlung, Fert.* **1973**, *28*, 201–211.

11. Withers, P.J.; Bhadeshia, H.K.D.H. Residual Stress Part 1—Measurement Techniques. *Mater. Sci. Technol.* **2001**, *17*, 355–365. [CrossRef]
12. Withers, P.J.; Bhadeshia, H.K.D.H. Resdiual Stress Part 2—Nature and Origins. *Mater. Sci. Technol.* **2001**, *17*, 366–375. [CrossRef]
13. Bhadeshia, H.K.D.H. *Handbook of Resdiual Stress and Deformation og Steel*; Chapter Material Factors; The Materials Information Society: Materials Park, OH, USA, 2002; pp. 3–10.
14. Hallberg, H.; Håkansson, P.; Ristinmaa, M. A constitutive model for the formation of martensite in austenitic steels under large strain plasticity. *Int. J. Plast.* **2007**, *23*, 1213–1239. [CrossRef]
15. Behrens, B.A.; Olle, P. Consideration of phase transformations in numerical simulation of press hardening. *Steel Res. Int.* **2007**, *78*, 784–790. [CrossRef]
16. Mahnken, R.; Schneidt, A.; Antretter, T. Macro modelling and homogenization for transformation induced plasticity of a low-alloy steel. *Int. J. Plast.* **2009**, *25*, 183–204. [CrossRef]
17. Behrens, B.A.; Olle, P.; Schäffner, C. *Process Simulation of Hot Stamping in Consideration of Transformation-Induced Stresses*; Numisheet: Melbourne, Australia, 2008; pp. 557–562.
18. Behrens, B.A.; Chugreev, A.; Chugreeva, A. FE-simulation of hot forging with an integrated heat treatment with the objective of residual stress prediction. In Proceedings of the 21st International ESAFORM Conference on Material Forming, Palermo, Italy, 23–25 April 2018; Volume 1960, p. 040003.
19. Simsir, C. 3D Finite Element Simulation of Steel Quenching in Order to Determine the Microstructure and Residual Stresses. Ph.D. Thesis, Middle East Technical University, Ankara, Turkey, 2008.
20. Simsir, C.; Gür, C.H. 3D FEM simulation of steel quenching and investigation of the effect of asymmetric geometry on residual stress distribution. *J. Mater. Process. Technol.* **2008**, *207*, 211–221. [CrossRef]
21. Denis, S.; Gautier, E.; Simon, A.; Beck, G. Stress-phase-transformation interactions—Basic principles, modelling and calculation of internal stresses. *Mater. Sci. Technol.* **1985**, *1*, 805–814. [CrossRef]
22. Mitter, W. *Umwandlungsplastizität und ihre Berücksichtigung bei der Berechnung von Eigenspannungen*; *Materialkundlich-Technische Reihe*, Gebrüder Bornträger Verlag: Berlin, Germany, 1987; Volume 7.
23. Mahnken, R.; Wolff, M.; Schneidt, A.; Böhm, M. Multi-phase transformations at large strains—Thermodynamic framework and simulation. *Int. J. Plast.* **2012**, *39*, 1–26. [CrossRef]
24. Mahnken, R.; Schneidt, A.; Antretter, T.; Ehlenbröker, U.; Wolff, M. Multi-scale modeling of bainitic phase transformation in multi-variant polycrystalline low alloy steels. *Int. J. Solids Struct.* **2015**, *54*, 156–171. [CrossRef]
25. Steinbach, I.; Pezzolla, F.; Nestler, B.; Seeßelberg, M.; Prieler, R.; Schmitz, G.; Rezende, J. A phase field concept for multiphase systems. *Phys. D Nonlinear Phenom.* **1996**, *94*, 135–147. [CrossRef]
26. Tiaden, J.; Nestler, B.; Diepers, H.; Steinbach, I. The multiphase-field model with an integrated concept for modelling solute diffusion. *Phys. D Nonlinear Phenom.* **1998**, *115*, 73–86. [CrossRef]
27. Steinbach, I.; Pezzolla, F. A generalized field method for multiphase transformations using interface fields. *Phys. D Nonlinear Phenom.* **1999**, *134*, 385–393. [CrossRef]
28. Steinbach, I.; Apel, M. Multi phase field model for solid state transformation with elastic strain. *Physica D* **2006**, *217*, 153–160. [CrossRef]
29. Steinbach, I. Phase-field models in materials science. *Model. Simul. Mater. Sci. Eng.* **2009**, *17*, 073001. [CrossRef]
30. Borukhovich, E.; Du, G.; Stratmann, M.; Boeff, M.; Shchyglo, O.; Hartmaier, A.; Steinbach, I. Microstrucutre Design of Tempered Martensite by Atomistically Informed Full-Field Simulation: From Quenching to Fracture. *Materials* **2016**, *9*, 673. [CrossRef]
31. OpenPhase. 2018. Available online: http://www.openphase.de/ (accessed on 1 August 2018).
32. Levitas, V.I.; Roy, A.M. Multiphase phase field theory for temperature- and stress-induced phase transformations. *Phys. Rev. B* **2015**, *91*, 174109. [CrossRef]
33. Levitas, V.I.; Roy, A.M. Multiphase phase field theory for temperature-induced phase transformations: Formulation and application to interfacial phases. *Acta Mater.* **2016**, *105*, 244–257. [CrossRef]
34. Schoff, E.; Schneider, D.; Streichhan, N.; Mittnacht, T.; Selzer, M.; Nestler, B. Multiphase-field modeling of martensitic phase transformation in a dual-phase microstructure. *Int. J. Solids Struct.* **2018**, *134*, 181–194. [CrossRef]

35.   Basak, A.; Levitas, V.I. Nanoscale multiphase phase field approach for stress- and temperature-induced martensitic phase transformations with interfacial stresses at finite strains. *J. Mech. Phys. Solids* **2018**, *113*, 162–196. [CrossRef]

36.   DIN EN ISO 683-17. *Heat-Treated Steels, Alloy Steels and Free-Cutting Steels—Part 17: Ball and Roller Bearing Steels*; Technical Report; Beuth-Verlag: Berlin, Germany, 2014.

37.   Weißbach, W.; Dahms, M.; Jaroschek, C. *Werkstoffkunde*; Springer Fachmedien: Wiesbaden, Germany, 2015.

38.   Rose, A.; Hougardy, P.H. *Atlas zur Wärmebehandlung der Stähle*; Verlag Stahleisen: Dusseldorf, Germany, 1972.

39.   DIN EN 15305:2009-1. *Non Destructive Testing—Test Method for Residual Stress Analysis by X-ray Diffraction*; Technical Report; Beuth-Verlag: Berlin, Germany, 2008.

40.   Eigenmann, B.; Macherauch, E. Röntgenographische Untersuchung von Spannungszuständen in Werkstoffen—Teil 3. *Materialwissenschaften Und Werkstofftechnik* **1996**, *27*, 426–437. [CrossRef]

41.   Voigt, W. *Lehrbuch der Kristallphysik*; BG Teubner: Wiesbaden, Germany, 1928.

42.   Reuss, A. Berechnung der Fließgrenzen von Mischkristallen auf Grund der Plastizitätsbedingung für Einkristalle. *Z. Angew. Math. Mech.* **1929**, *9*, 49–58. [CrossRef]

43.   Behrens, B.A.; Chugreev, A.; Kock, C. Experimental-numerical approach to efficient TTT-generation for simulation of phase transformations in thermomechanical forming processes. In *IOP Conference Series: Materials Science and Engineering*; IOPScience: London, UK, 2018; Volume 461, p. 012040.

44.   Acht, C.; Dalgic, M.; Frerichs, F.; Hunkel, H.; Irretier, A.; Lübben, T.; Surm, H. Ermittlung der Materialdaten zur Simulation des Durchhärtens von Komponenten aus 100Cr6. *J. Heat Treat. Mater.* **2008**, *63*, 234–244. [CrossRef]

45.   JMatPro. Practical Software for Materials Properties. 2018. Available online: https://www.sentesoftware.co.uk/jmatpro (accessed on 1 August 2018).

46.   Saunders, N.; Guo, U.K.Z.; Li, X.; Miodownik, A.P.; Schillé, J.P. Using JMatPro to Model Materials Properties and Behavior. *JOM* **2003**, *55*, 60–65. [CrossRef]

47.   Guo, Z.; Saunders, N.; Schillé, J.P.; Miodownik, A.P. Material properties for process simulation. *Mater. Sci. Eng. A* **2009**, *1–2*, 7–13. [CrossRef]

48.   Special Metals Co. New Hartford, New York, USA. 2018. Available online: http://www.specialmetals.com/assets/smc/documents/pcc-8064-sm-alloy-handbook-v04.pdf (accessed on 1 August 2018).

49.   Hensel, A.; Spittel, T. *Kraft- und Arbeitsbedarf Bildsamer Formgebungsverfahren*; Deutscher Verlag für Grundstoffindustrie: Berlin, Germany, 1978.

50.   VDI-Gesellschaft Verfahrenstechnik und Chemieingenieurwesen. In *VDI Wärmeatlas*; Springer: Berlin/Heidelberg, Germany, 2006.

51.   DIN EN ISO 6507-1. *Metallic Materials—Vickers Hardness Test—Part 1: Test Method*; Technical Report; Beuth-Verlag: Berlin, Germany, 2018.

52.   Bhattacharya, K. *Microstructure of Martensite: Why It Forms and How It Gives Rise to the Shape-Memory Effect*; Oxford University Press: Oxford, UK, 2003.

53.   Mosler, J.; Shchyglo, O.; Hojjat, H.M. A novel homogenization method for phase field approaches based on partial rank-one relaxation. *J. Mech. Phys. Solids* **2014**, *68*, 251–266. [CrossRef]

54.   Kiefer, B.; Furlan, T.; Mosler, J. A numerical convergence study regarding homogenization assumptions in phase field modeling. *Int. J. Numer. Methods Eng.* **2017**, *112*, 1097–1128. [CrossRef]

55.   Bartels, A.; Mosler, J. Efficient variational constitutive updates for Allen-Cahn-type phase field theory coupled to continuum mechanics. *Comput. Methods Appl. Mech. Eng.* **2017**, *317*, 55–83. [CrossRef]

56.   Sarhil, M. Constitutive Relations and Homogenization Assumptions in Phase-Field Models with Elasticity: Martensite Transformation as an Example. Master's Thesis, Universität Duisburg-Essen and Ruhr-Universität Bochum, Essen, Germany, 2018.

57.   Simo, J.; Hughes, T. *Computational Inelasticity*; Springer Verlag: Berlin, Germany, 1998.

58.   Miehe, C. *Kanonische Modelle Multiplikativer Elasto-Plastizität—Thermodynamische Formulierung und Numerische Implementation*; Forschungs- und Seminarberichte aus dem Bereich der Mechanik der Universität Hannover: Hannover, Germany, 1992.

59. Miehe, C.; Schröder, J.; Schotte, J. Computational homogenization analysis in finite plasticity. Simulation of texture development in polycrystalline materials. *Comput. Methods Appl. Mech. Eng.* **1999**, *171*, 387–418. [CrossRef]

60. Schröder, J. *Plasticity and Beyond—Microstructures, Crystal-Plasticity and Phase Transitions (CISM Lecture Notes 550*; Schröder, J., Hackl, K., Eds.; Chapter A Numerical Two-Scale Homogenization Scheme: The FE^2-Method; Springer: Berlin, Germany, 2014; pp. 1–64.